Excited-state Dynamics of Metal Nanostructures Studied by Ultrafast Near-field Spectroscopy

HuiJun Wu

DOCTOR OF PHILOSOPHY

Department of Structural Molecular Science
School of Physical Science

The Graduate University for Advanced Studies

2012

Contents

Abstract

Ultrafast nano-optics is a rapidly growing research field aiming at probing, manipulating and controlling ultrafast optical excitations on nanometer spatial scales. The ability to control light on nanometric spatial and femtosecond time scales opens up exciting possibilities for probing dynamic processes in nanostructures in real time and space.

A wide variety of elementary physical processes occur on femtosecond time and nanometric spatial scales. Recently, the surface plasmon resonance (SPR) excitations in noble metallic nanostructures, occurring on time scales of < 20 fs and spatial scales ranging from a few nm to tens of micrometer, have attracted increasing attention, due to their broad application fields, such as developing optical communication devices, ultrasensitive analytical methods, and biosensors.

In order to get a deeper understanding of the spatial and temporal characteristics of SPR, the ultrafast scanning near-field optical microscope (SNOM) system has unique advantages. We developed an ultrafast SNOM system, by combining ultrafast time-resolved techniques with near-field method, which enables us to perform ultrafast measurement of nanomaterials with very high spatial resolution.

In optical-fiber-probe-based apertured SNOM system, pulse broadening due to the group velocity dispersion (GVD) effect is serious, since an optical fiber with a length of tens of cm is used for the fiber probe. In addition to the optical fiber, various optical elements used in the optical system also introduce GVD. Furthermore, for light pulses as short as 20 fs or less, not only linear dispersion but also higher order dispersion effects become dominant. The higher-order GVD effects further seriously degrade the time resolution of the SNOM system. Therefore, a sophisticated dispersion compensation system is necessary to remove the linear and higher-order

GVD, and hence to achieve very high time resolution.

To achieve ultrafast time resolution (20 fs or higher) that enables direct observation of plasmon dynamics, we constructed GVD compensation system based on combination of a prism pair device, a grating pair device, and a pulse-shaping device consisting of a deformable mirror (DFM) and a grating (4-f system). We found that a combination of all these three devices is necessary in order to fully remove the GVD arising from a 15-cm optical fiber and the other optical components used in the SNOM system.

By adjusting the grating and prism pairs, the major part of the linear GVD and partially the higher-order GVD could be compensated. The remaining GVD could be removed by optimizing the surface shape of the DFM in an iterative manner, which was controlled by a genetic algorithm, using the second harmonic (SH) photons of the ultrashort pulses generated at the sample position as a feed back signal. With this method, we succeed in compressing the pulses as short as ~17 fs at the probe tip, with ~100 nm (or higher) spatial resolution in the SNOM system.

We also performed time-correlated two-photon-induced photoluminescence (TPI-PL) measurements for a gold nanoparticle to demonstrate the performance of the SNOM system. The pump-probe technique enables a direct measurement of the dynamical properties in the time domain. A pump pulse stimulates electrons out of the valence band into unoccupied states with energies between Fermi and vacuum levels to excite plasmon oscillation. A subsequent probe pulse further excites the plasmon to higher level to induce photoluminescence. The photoluminescence yield depends on the transient population of the resonant intermediate plasmon state of the photoexcitation by the pump pulse. The measured time-resolved pump-probe signal contains information on the dephasing time of SPR.

We also performed the time-correlated TPI-PL measurement at the center position

of a gold nanoparticle. The gold nanoparticle sample was prepared by an electron-beam lithography method on a glass substrate, with the typical size of 110 nm (length) × 90 nm (width) × 15 nm (thickness). The emission in the wavelength region <720 nm was detected and the intensity was recorded as a function of the pump-probe delay time. We found that the half-width of the time-correlated TPI-PL trace was longer than that of the autocorrelation trace of the pump/probe pulse measured by the SH signal. This is due to the finite decay time of the SPR. We adopted a model to simulate the time-resolved profile and found the dephasing time to be 8±3 fs based on a fitting procedure. This is the fastest dynamics of a single-particle material ever observed in the time-domain by SNOM.

Abbreviations

SNOM：scanning near-field optical microscope

SPR：surface plasmon resonance

AFM：atomic force microscope

SEM：scanning electron micrograph

STM：scanning tunneling microscope

PMT：photo-multiplier tube

BBO：β-barium borate

DFM：deformable mirror

GVD：group velocity dispersion

TPI-PL：two-photon-induced photoluminescence

FWHM：full width at half maximum

SHG：second harmonic generation

GA：genetic algorithm

Chapter 1

Introduction and background of the study

1.1 History of Scanning Near-field Optical Microscope

The ability to view and investigate very small samples under high magnification is indispensable in many research fields such as the biological sciences, microelectronics, and materials research [1-6]. Optical techniques are widely used for the purposes of getting information on ultrafast dynamics. However, the spatial resolution of conventional optical microscopy is limited to approximately half of the wavelength of the light used. This limitation is theoretically explained by the diffraction limit of light. When a light beam is focused with a lens, the focused light forms a diffraction pattern consisting of concentric circles at the focal point. In 1873, Ernst Abbe first described this phenomenon theoretically in detail [7]. He used the spacing between the concentric rings to define the resolution limit.

$$d = 0.61(\lambda_0 / n \sin \theta) \tag{1.1}$$

where d is the distance between rings, λ_0 is the wavelength of light in vacuum, n is the refractive index of the medium, and θ is the convergence angle of the focusing optical beam. The factor $n \cdot sin\theta$ is commonly known as the numerical aperture (NA). NA can be increased up to 1.3-1.4 with high indices of refraction media such as immersion oils. Therefore, Eq.1 is usually simplified to $d \sim \lambda/2$. In actual cases, the resolution is lowered sometimes because of aberrations due to the optical components and other experimental reasons. This means that the resolution is limited to ~200 nm if we use visible light for observation. This limitation of resolution prohibits the investigation of nanoscale phenomena by optical methods.

This limitation motivated the development of higher resolution techniques such as scanning electron microscopy (SEM) [8] and transmission electron microscopy (TEM) [9], and later various scanning probe microscopies such as atomic force microscopy

(AFM) [10] and scanning tunneling microscopy (STM) [11]. These methods have made it possible to image even single atoms.

Although these newly developed microscopic methods succeeded in improving spatial resolution, they cannot gain the benefits of spectroscopic information. They also sometimes require specific sample preparation and/or conditions such as high vacuum, which reduces flexibility in possible working environments.

The development of SNOM has actually met many technical challenges. One of the most essential point is that in the near-field region of an irradiated sample ($\leq \lambda/4$ from sample), high spatial frequency components of the light field emit radiation as exponentially decaying waves, which typical far-field detectors are not able to sense. In order to detect the near-field radiation, Synge proposed the use of a sub-wavelength aperture at the position of the near-field to be detected in the vicinity of the sample to collect the evanescent waves [12]. By using a nanometer-scale aperture probe, the non-radiating near-field waves could be converted into propagating waves which can be collected by a photodetector. However, Synge noticed that several technical problems must be solved in order to make his idea come to reality, such as preparation of very sharp glass probes, making sub-wavelength apertures, and nanometer-scale positioning techniques.

The first demonstration of high spatial-resolution imaging using a sub-wavelength aperture was performed by Ash and Nicholls in 1972 [13], who used the microwave radiation. They obtained $\lambda/60$ spatial resolution for the measurement of a metal grating sample, by using a 3-cm wavelength microwaves as a light source.

In1986, Binnig and Rohrer invented the scanning tunneling microscope (STM), in which they developed a technology to manipulate a metallic tip within Angstroms from a conducting surface [14]. With this nanometer-precise positioning method, Aaron Lewis and his co-workers could first demonstrated the optical measurement

with sub-diffraction limit resolution [15]. Pohl's laboratory also independently created an optical microscope based on Synge's idea [16]. They also proposed a preparation method of a probe tip with a sub-wavelength aperture and a feed-back loop method to maintain a constant gap between the tip and the sample surface. All of these technical advances made the SNOM a reality.

The SNOM system could be basically categorized into illumination mode, collection mode, and illumination-collection mode, depending on the configuration and types of probes adopted. In illumination mode, the probe tip illuminates the sample and transmitted light or fluorescence is collected from beneath the transparent sample. In collection mode, the sample is illuminated from the far-field and the probe is used to collect light. As for illumination-collection mode, the probe illuminates the sample and the light is collected back through the same probe, and this mode is useful for investigation of opaque samples [17].

1.2 Ultrafast Scanning Near-field Optical Microscope

There are a wide variety of elementary physical processes occur on femtosecond time scale in nanoparticles, such as the propagation of electronic wave packets in semiconductor nanostructrue [18-19], energy transport and electron transfer processes in organic semiconductor [20-21]. In recent years, the dynamics of surface plasmon resonance (SPR) excitation in metallic nanostructures, typically occurring on time scales of 1-100 fs and in the spatial scale of a few nanometers to micrometers, has attracted much interest and has been intensively and widely studied [22-23]. Deep understanding of the above-mentioned phenomena demands a simultaneous direct space- and time-resolved imaging technique.

Time-resolved electron microscopy techniques are rapidly developed recently, but

presently the resolution is limited in ps to sub-ps regime [18-21]. The situation is similar for diffraction-based techniques, such as ultrafast election and X-ray diffraction methods [24-26], and these techniques are applicable only to ensembles of atoms and molecules (or nanomaterials). Developments of new experimental techniques that can investigate the dynamics of optical excitation in individual nanostructures on femtosecond time and nanometric spatial scales are indispensable. It may become a useful technique for the studies of excited-state dynamics of nanomaterials if we can combine the high time-resolution afforded by the optical/spectroscopic techniques, with high-spatial resolution microscopic methods. Development of ultra-fast SNOM, which enables optical measurements with a spatial resolution beyond the classical diffraction limit, was motivated by this idea [27-35].

The high spatial-resolution in SNOM was achieved as mentioned in the previous section. The challenge comes to get a temporal resolution in a femtosecond regime in the SNOM. The ultimate time resolution cannot be obtained only by introducing a laser source with femtosecond pulse duration. A few of methods have been proposed to achieve the purpose, including localizing ultrafast laser pulse to the apex of ultra-sharp metal tapers [36-38], or passing the laser pulse through a hollow-pyramid type aperture near-field probes [40]. As for the use of ultra-sharp metal tapers, the time resolution is limited by the finite spectral width of the SPR in the scattered light spectrum of the tapered tips. For the hollow-pyramid type near-field aperture probe, there remains difficulty in preparing a probe with high throughput and high spatial resolution. In this thesis, we adopt an aperture-type optical fiber based near-field probe. Our group previously built a SNOM system with ~100 fs time resolution and obtained results on the study of SPR in single gold nanoparticle [31, 32]. However, this time resolution is not enough to further clarify

12

the detailed behavior of plasmon dynamics, especially the dephasing. As is well known, the optical fiber introduces a large amount of group velocity dispersion (GVD), and consequently a 15-fs laser pulses are broadened to several picoseconds after propagating through a 100-mm optical fiber. If we adopt a well-designed GVD compensator, on the other hand, the GVD can be fully removed and hence we may get enough high time resolution at the probe tip. The development of GVD compensators optimized for the fiber-probe-based SNOM will be described in detail in the following chapters.

One of the typical optical fiber based ultra-fast SNOM setup is shown in Figure 1.1. An illumination-mode configuration is adopted here. Pulses from a femtosecond Ti:sapphire laser are split into two parts by a beam splitter, with an intensity ratio of 1:1. The two beams are combined again and then incident into a GVD compensator to pre-compensate the GVD arising from all the optical components involved. The laser pulse is then coupled to an optical fiber that has an aperture probe at another end.

The tip is mounted onto a mechanical block that includes adjustment screws to approach the probe tip close to the surface of the sample. After the tip is approached to the sample surface within the range of the Z-axis piezo-stage displacement, a shear force feedback method is turned on to control the gap between the tip and the sample surface to be a few nanometers. The probe is driven by a dithering piezo stage and oscillates at a resonant frequency, and moved closer to the surface, while the oscillation amplitude is detected by shining an infrared laser on the probe and measuring the reflected signal with a photodiode. The oscillation of the probe will be damped as it approaches to the surface and in this way the probe tip can be maintained within few nm from the sample surface by the feedback method. The shear force feedback is also used to obtain a topographic image analogous to that
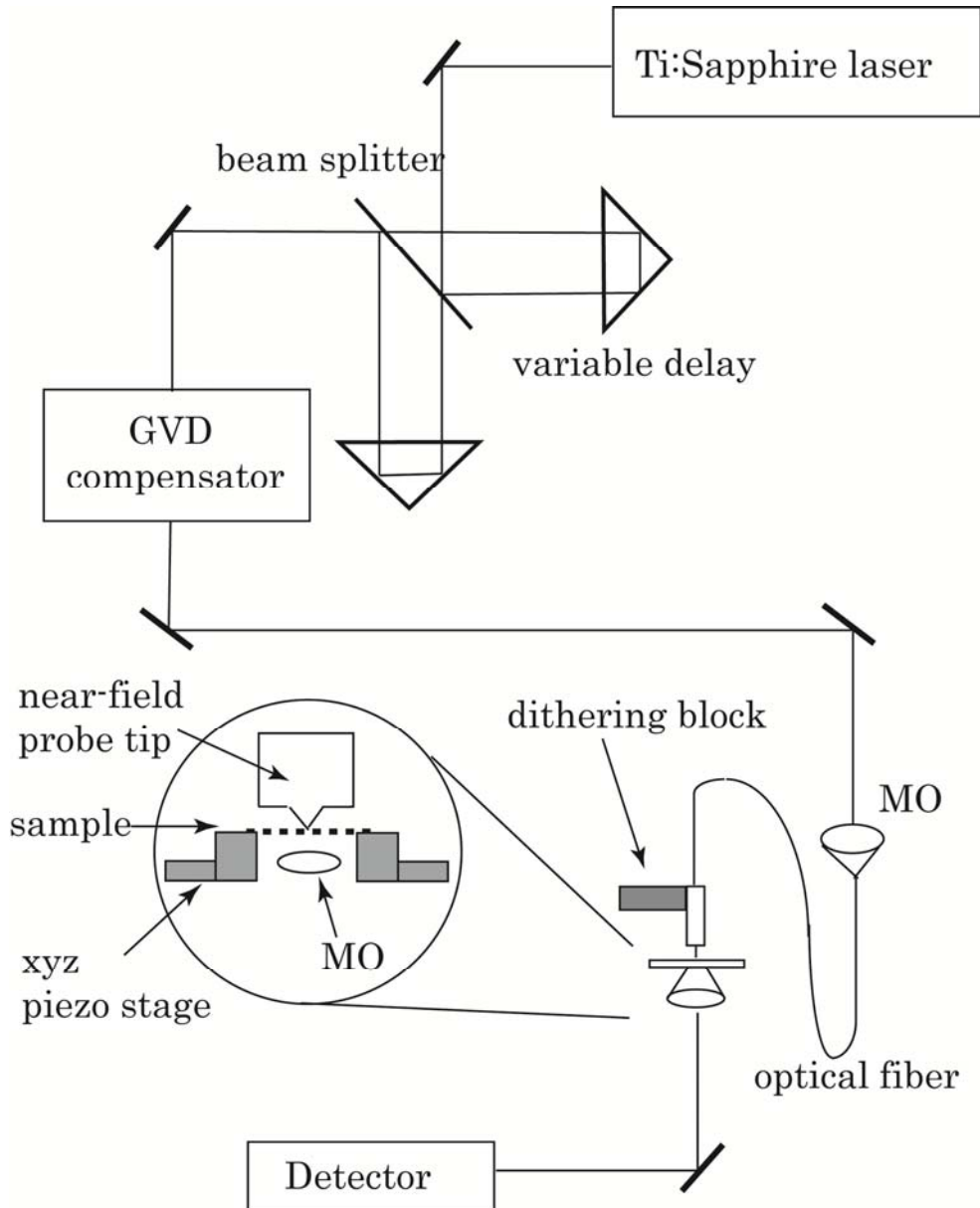
Fig. 1.1 Schematic setup of an ultrafast scanning near-field optical microscope. MO: micro objectives.

obtained with an AFM.

Beneath the sample, an objective lens with a high NA value (>0.8) was set to collect the luminescence emitted from the sample. A photo-multiplier tube (PMT) or photon counting photodiode was used to detect the optical signal. The ultrafast SNOM system could be used to investigate various kinds of ultrafast dynamics in nanomaterials. In this thesis, we mainly focus on the research of surface plasmon

dynamics of gold nanoparticles.

1.3 Surface plasmon dynamics

When a metal nanostructure is shined by light, the conduction electrons within the penetration depth of the excitation from the metal surface translate collectively with respect to the lattice of the positive charges. The attractive forces between negative charges of the electrons and positive charges of lattice ions give a restoring force for the collective motion resulting in a collective oscillation of the electrons. The collective oscillation of the conduction electron that typically occurs at the surface of metal nanostructures is called surface plasmon resonance (SPR). The individual electrons move stochastically but a superstition of many independent electron oscillations yields collective oscillation of electrons. The collective oscillation of electrons damps via radiative and nonradiative damping (T_1 process described later) and via randomization of the phase relations among individual electron oscillations by elastic collisions (T_2^* process). The resonance frequency of the oscillation is controlled by the microscopic restoring force, as well as by dielectric environment determined by the particle size, shape and the surrounding medium. Many works were devoted to studies on the characteristics of SPR as a function of particle size, shape and dielectric properties, while more detailed behavior of ultrafast dynamics of SPR for a single metallic particle have still remained to be revealed [39-42].

Excitation and relaxation of SPR in metallic nanoparticles play an important role in linear and nonlinear optical effects of them, such as the extinction spectral characteristics, local field enhancement, and so forth. The studies of dynamic behavior of SPR in the time-scale from a few femtoseconds to several picoseconds help us to get fundamental knowledge about the basic properties of the light-matter interaction in metallic nanoparticles. One of essential issue among them is how fast the collective excitation loses their phase coherence, and what is the internal

mechanism that controls this procedure.

Generally speaking, the energy relaxation of materials proceeds in several steps [43]. Initially, the electrons absorb the energy of photons via interband and/or intraband transitions. The resultant electron distribution is highly non-thermal and strongly correlated in the time scale of few femtoseconds. After the phase coherence of the excitation is lost, the first energy relaxation step is the electron thermalization by electron-electron scattering, which establishes a new Fermi electron distribution with a higher temperature than that before photoexcitation. The energy is transferred into quasi-particle pairs (electron hole pairs). The electron-electron scattering redistributes the excitation energy to thermalize the electron gas. Quasi-elastic electron-phonon and electron-surface scattering do not play a dominant role in this stage in the dissipation of the excess energy of laser excited hot electrons. Fan and co-workers have shown, through the time resolved photoemission experiment for a gold film, that the temporal scale of this thermalization process is of a few hundreds of femtoseconds [44].

Then the thermalization process to the lattice occurs as the next step. The energy is transferred from the hot electron system to the relatively cold lattice of the nanoparticles. This process has been studied in detail for thin films made of various noble metals. In general, it takes about a few ps until a quasi-equilibrium state is formed between the electron system and the lattice (phonon) system. This heat-exchange process is also described as the electron-phonon coupling process [45-49].

The last step in the energy relaxation is the heat transfer between the nanoparticles and the surrounding medium. The relaxation occurs in a time scale of several ps to hundreds of ps. This process is sensitive to the thermal conductivity of the surrounding medium. In this time region, the lattice temperature of the

16

nanoparticles is considered to be the same as the electron temperature [50-52].

The dephasing procedure of SPR, of which time constant is usually denoted as T_2, takes place in the first step of relaxation immediately after the photoexcitation which consists of inelastic decay process (time constant T_1) and the pure dephasing (time constant T_2^*). The first part is a decay due to the energy transfer from plasmon into formation of electron-hole pairs or reemission of photons (radiation damping), while the second is a randomization of the phase relations among the individual electron oscillations due to elastic collisions [53]. The relationship among them is given in Equation (1.2):

$$\frac{1}{T_2} = \frac{\Gamma}{2 \cdot h} = \frac{1}{2 \cdot T_1} + \frac{1}{T_2^*} \tag{1.2}$$

where Γ is the homogeneous linewidth of the plasmon resonance.

Many experiments have been performed in order to determine dephasing times of metal nanopartilces. Lamprecht measured the dephasing time for lithographically prepared gold nanoparticles using a second-order nonlinear optical autocorrelation method in the femtosecond regime at far-field. The obtained dephasing time was found to be 7 fs for ~200 nm gold nanoparticles [54-55].

Since size and shape distribution of the nanoprticles affects the measurements of dephasing times in ensemble measurements, it is advantageous to perform the measurement on single nanoparitcles. Liau and his co-workers performed the second-order interferometric autocorrelation measurement on single silver nanoparticles by combining an optical microscope with an AFM. They got a dephasing time of 10 fs for 75 nm silver nanoparticles [56].

Another way to estimate dephasing times while overcoming the problem of inhomogeneous broadening due to variations of size and shape is to adopt the

single-particle spectral width measurements. Klar et al. performed the near-field transmission spectral measurement on gold nanoparticles with averaged size of 40 nm. They extracted the dephasing time from the homogeneous linewidth, which was around 8 fs [57]. Soennichsen et al. investigated the dephasing time of single gold nanorods based on single-particle light-scattering spectroscopy, and observed the dephasing time ranging from a few fs to 20 fs depending on the aspect ratio of the nanorods [58]. Spectral hole burning is another technique used to investigate the dephasing time in metallic nanoparticles. By subtracting the absorption spectrum of nanoparticles before and after the laser irradiation, the decay time was found to be 4.8 fs for silver nanoparticles with the radius of 7.5 nm [59].

As mentioned above, experimental investigations on dephasing of noble metal nanoparticles have been performed via time-domain measurements of ensembles of particles or frequency-domain light scattering spectral measurements of ensembles or single particles [54-59]. With ultrafast SNOM method, we can study the single-particle plasmon dynamics in the time domain (possibly even position dependence measurements in a single particle) with very high time and spatial resolution.

1.4 Ultrafast Measurement Technique

1.4.1 Principle of pulse duration measurement

In this section, the principle of pulse duration measurement (and that of dephasing measurements in the following subsection) is briefly explained. In the ultrafast SNOM system, the time resolution is determined by the pulse duration at the probe tip. Although principle of the measurements is explained for the far-field

measurement, the basic idea is applicable to the near-field measurement as described in Section 3.
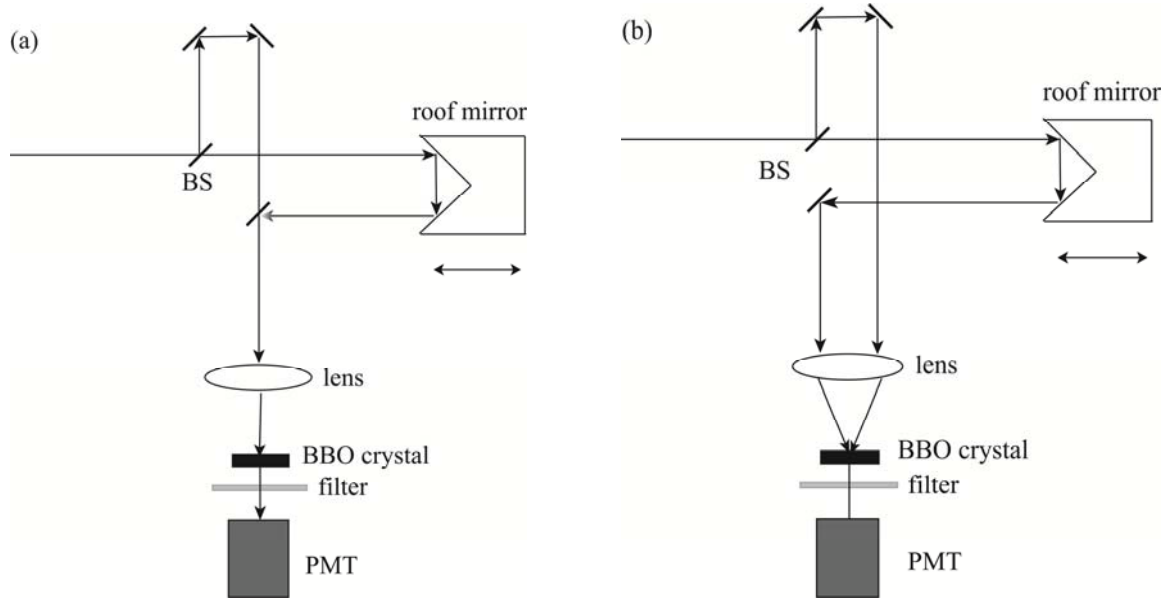

Fig. 1.2 Basic experimental setup of second-order autocorrelation measurement. (a) Collinear configuration and (b) non-collinear configuration. BS: beam splitter, PMT: photo multiplier tube.

The characterization of the temporal profile of the laser pulse is the basis of any ultrashort laser optimization and the prerequisite of any ultrafast measurements. However, response times of photoelectric devices are generally limited to nano to picosecond regime and therefore the optical methods based on autocorrelation techniques should be adopted. There are several conventional methods of autocorrelation measurements, such as intensity autocorrelation, and fringe-resolved autocorrelation. In this work, we mainly utilized the fringe-resolved autocorrelation method to determine the pulse duration [60].

In the autocorrelation methods, the laser beam is split into two identical beams by a beam splitter as shown in Fig. 1.2. One of the two pulses is delayed from the other for a variable time delay τ. The beams of the two arms are collinearly recombined (in the case of collinear configuration) and are then focused onto a thin nonlinear crystal,

such as a BBO crystal. The autocorrelation trace is then recorded by plotting the second harmonic intensity as a function of τ.

The expression for the second-harmonic intensity under the collinear configuration is given as

$$I\ (\tau) = \int_{-\infty}^{+\infty} \left| [E(t) + E(t - \tau)]^2 \right|^2 dt = \int_{-\infty}^{+\infty} \left| E(t)^2 + 2E(t)E(t - \tau) + E(t - \tau)^2 \right|^2 dt \quad (1.3)$$

where $E(t)$ and $E(t-\tau)$ are the electric fields for the two arms of the interferometer, respectively, and τ is the time delay between two arms.

We can then obtain the intensities of the signal in the cases $\tau = 0$ and $\tau = \infty$ as, for a Fourier-transform-limited optical pulse.

$$I(\tau = 0) = 2^4 \int E^4(t) dt \qquad (1.4)$$

$$I(\tau = \infty) = 2 \int E^4(t) dt \qquad (1.5)$$

The ratio between the intensities at $\tau = 0$ and $\tau = \infty$ should be 8:1 in this case. If the pulse is chirped, regardless whether with linear or nonlinear chirp, this ratio is decreased. This can be used as a criterion to judge whether the pulse is chirped or not.

There is a relationship between the full width at half maximum (FWHM) Δt of the autocorrelation trace and the real pulse duration $\Delta \tau$ depending on the pulse shape. In order to know the real pulse duration, we first have to assume a realistic pulse shape. Table1.1 summarized the relation between Δt and $\Delta \tau$ for some typical pulse shapes. The sech^2 pulse shape is commonly adopted as a realistic one for mode-locked laser outputs. This assumption for the pulse shape will be also adopted

in this thesis. In this case $\Delta\tau/\Delta t$ is set to be 1.54.

$I(t)$	Δt	$\Delta\tau$	$\Delta\tau/\Delta t$
e^{-t^2}	1.665	2.355	1.414
$\mathrm{sech}^2(t)$	1.763	2.72	1.543
$\dfrac{1}{e^{t/(t-A)} + e^{-t/(t-A)}}$ A=1/4	1.715	2.648	1.544
A=1/2	1.565	2.424	1.549
A=3/4	1.278	2.007	1.570

Table 1.1 Relationships between autocorrelation FWHM $\Delta\tau$ and pulse intensity FWHM Δt.

1.4.2 Principle of SPR dephasing time measurement

As discussed in Section 1.2, there are various ways to estimate the dephasing time of SPR in the metal nanoparricles, either directly in the time-domain or indirectly in the frequency-domain. In the present work, we adopted time-correlated two-photon-induced photoluminescence (TPI-PL) method, which enables a pump-probe technique to directly measure the dephasing time in the time domain [61-63].

The principle of time-correlated TPI-PL is schematically shown in Fig 1.3. A pump pulse $E(t)$ is incident on the metal nanoparticle (the pulse is assumed to be centered at $t = 0$), which excites the nanoparticle to a plasmon resonance state. Subsequently, a probe pulse $E(t-\tau)$ photoexcites the particle after a delay time of τ to a higher level, which emits photoluminescence in the wavelength region shorter than the incident light. The emitted photoluminescence yield is determined by the transient

population of the plasmon-resonant intermediate state and the relative phase of the
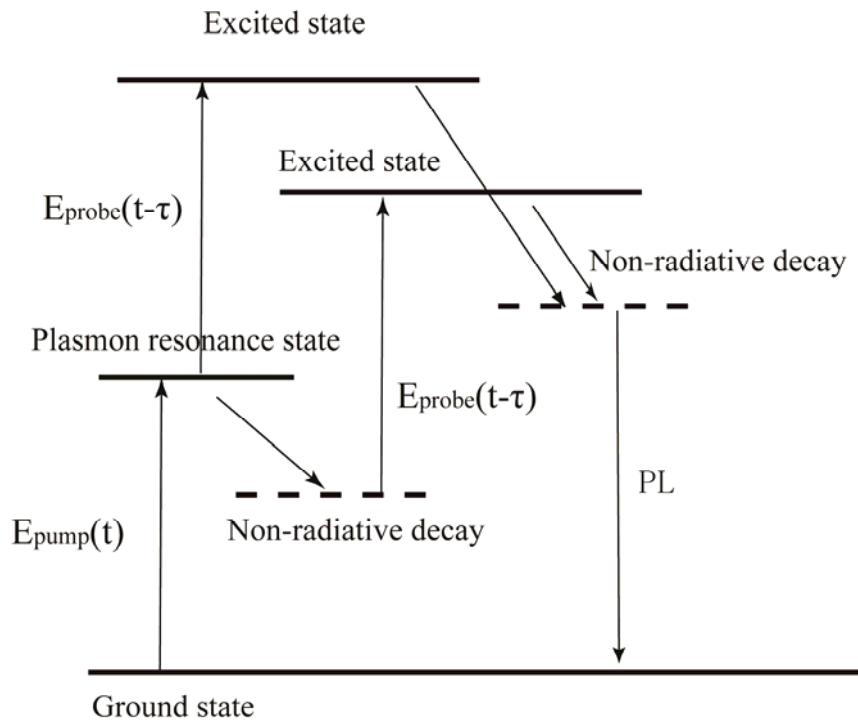

Fig 1.3 Mechanism of the time-correlated TPI-PL. PL indicates the photoluminescence.

probe field with respect to the plasmon oscillation, which depend on the pump-probe time delay. The measured time-correlated TPI-PL signal contains the information on the dephasing of SPR, which is reflected on the width of the TPI-PL correlation profile. The incident laser field induces a plasmonic field on the surface of a gold nanoparticle, which is a convolution of the laser filed and response function of the surface plasmon. This response function of the surface plasmon decays with a dephasing time τ. Consequently, the plasmonic field lasts longer than the laser field, as illustrated in Fig 1.4 based on the formula given below. Since the TPI-PL process is governed by the plasmonic field, the TPI-PL correlation profile is broadened due to the finite dephasing time.

Lamprecht et.al proposed a model to analyze the influence of plasmon dephasing on the FWHM of the time-correlated TPI-PL profile [64, 65]. In this model the plasmon field $E_{Pl}(t, \tau)$ of a single particle for a given pulse delay time τ is defined as
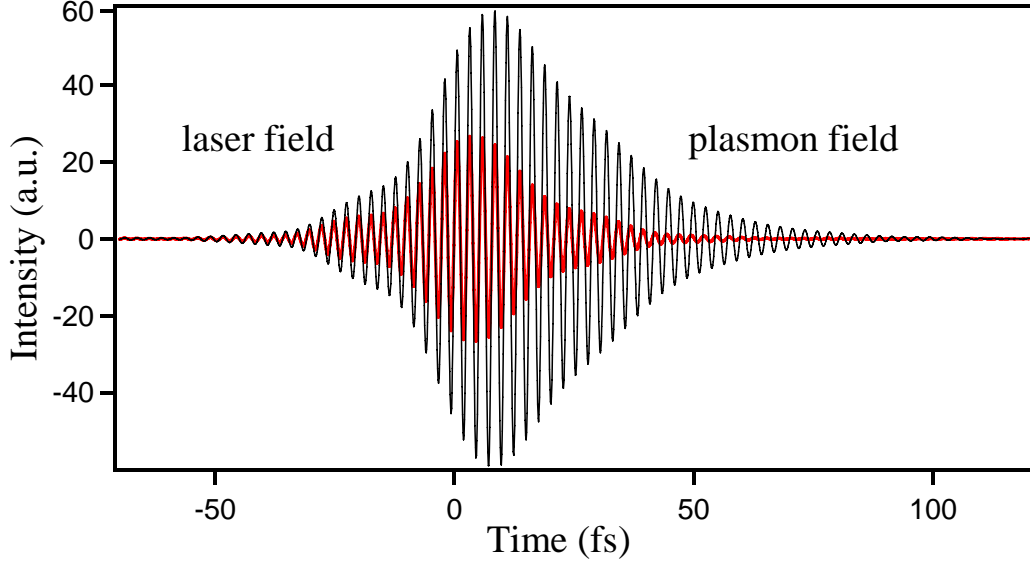
22

Fig1.4 Temporal behavior of pulse laser field (red) and the resonantly driven plasmon field (black).

$$E_{\mathrm{Pl}}(t;\tau) \approx \int_{-\infty}^{t} \frac{1}{\omega_0} K(t^*,\tau) e^{-\gamma(t-t^*)} \sin\left[\omega_0(t-t^*)\right] dt^* \tag{1.6}$$

with

$$K(t^*,\tau) = E(t^*) + E(t^*-\tau), \quad \omega_0 = \frac{2\pi c}{\lambda_{\mathrm{res}}}, \quad \gamma = \frac{1}{2\pi\tau_{\mathrm{dp}}}$$

where λ_{res} denotes to the resonance wavelength, c the speed of light, and τ_{dp} is the dephasing time of SPR. We can then calculate the time-resolved correlation signal profiles based on Equation (1.6) for given dephasing times τ_{dp}. By comparing the measured TPI-PL autocorrelation profile with the simulated curve, the depahsing time of SPR can be estimated.

Chapter 2

GVD arising from optical components and devices generating negative GVD

2.1 Introduction

Since various dispersive media are used as optical components in SNOM, the time resolution of ultrafast measurements in SNOM is usually deteriorated due to GVD arising from the optical fiber as well as other optical elements. Ultrashort pulses are seriously broadened by the GVD effects. Fig. 2.1 shows a typical example of pulse broadening where an autocorrelation trace is plotted for 15-fs laser pulses after passing through a 150 mm length optical fiber. The FWHM of the autocorrelation trace is around 6 ps, which means that the pulse duration was elongated for several orders after passing through the optical fiber. Such a broadened pulse cannot be used for the ultrafast measurements in the SNOM.
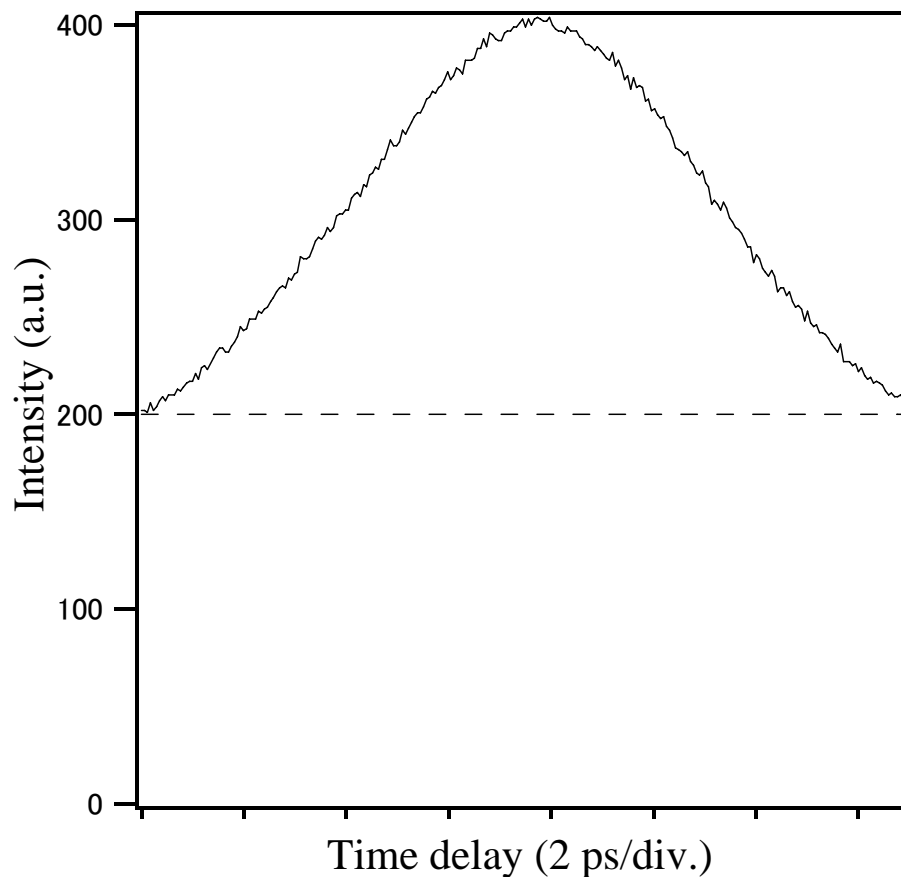
Fig. 2.1 Autocorrelation trace of a 15-fs pulses propagated through a 150 mm optical fiber.

In order to obtain very short pulse duration at the probe tip of the SNOM, this huge GVD must be removed by some means. There are several methods to remove the GVD, including the passive devices such as prism pair [66] and grating pair [67], and active pulse shaping techniques, for instance, by using liquid-crystal modulators [68], acousto-optic modulators [69] and deformable mirror (DFM) [70]. Each of them has their own unique characteristics, and can be used for different purposes. The characteristics of prism pair, grating pair, and DFM will be discussed in the following subsections. In this thesis, the combination of these three devices was finally adopted for the ultrafast SNOM.

Before performing any actual experiments, we estimate how much positive GVD optical fibers generate, and how much negative GVD the above-mentioned devices can introduce.

2.2 Estimation of GVD arising from the optical fiber

For a single-mode optical fiber used in the near-field probe, the material dispersion is the dominant reason for pulse broadening, which is caused by the wavelength dependence of the refractive index of the material. The intensity dependence of the refractive index also leads to nonlinear effects due to the self-phase modulation [71, 72] if the peak intensity of the incident laser is high, but such nonlinear effects are not serious in the present case and not considered in this thesis. The refractive index of doped silica (the material used for single-mode optical fibers) can be approximately described by the empirical Sellmeier equation [73]:

$$n^2(\lambda) - 1 = \sum_{j=1}^{3} \frac{A_j \lambda^2}{\lambda^2 - B_j} \qquad (2.1)$$

Dopant (%)	A_1	A_2	A_3	B_1	B_2	B_3
GeO$_2$ (0%)	0.696	0.408	0.897	0.00468	0.0135	97.9
GeO$_2$ (6.3%)	0.708	0.420	0.866	0.00792	0.0105	97.9
GeO$_2$ (19.3%)	0.735	0.446	0.808	0.00585	0.0155	97.9

Table 2.1 Coefficients of Sellmier equation for GeO$_2$-doped fused silica

Dopant	$n(\lambda)$	$dn/d\lambda$ /10^4 m^{-1}	$d^2n/d\lambda^2$ /10^{11} m^{-2}	$d^3n/d\lambda^3$ /10^{18} m^{-3}	$d^2\psi/d\omega^2$ /10^4 fs^2	$d^3\psi/d\omega^3$ /10^4 fs^3
GeO$_2$ (0%)	1.4533	-1.7	0.4	-0.2	0.5435	0.1062
GeO$_2$ (6.3%)	1.488	-1.788	0.459	-0.23	0.6691	0.2666
GeO$_2$ (19.3%)	1.5248	-1.968	0.582	-0.291	0.7655	0.3352

Table 2.2 Dispersion parameters of silica doped with GeO$_2$ at λ = 800 nm and GVD for optical fibers (150 mm) made of respective materials.

where n is the refractive index, λ is the wavelength in unit μm, A_j and B_j are experimentally determined Sellmeier coefficients. Note that this λ is the vacuum wavelength, not that in the material itself.

Since we have no detailed information on materials of the optical fiber for the near-field probe, we assume here that the optical fiber is made of fused silica doped with GeO$_2$. The corresponding values of the coefficients A_j and B_j for doped fused silica are summarized for a few of dopant concentration in Table 2.1 [74, 75].

By using the Eq. (2.1) with the coefficient in Table 2.1, the value of $n(\lambda)$ at a specific wavelength for an optical fiber can be estimated. The values of $dn/d\lambda$ and $d^2n/d\lambda^2$ can also be obtained consecutively. The dispersion parameters are shown in Table 2.2 [76]. We can then calculate the second-order GVD for the optical fiber according to the equation [77],

$$\frac{\mathrm{d}^2\psi}{\mathrm{d}\omega^2} = \frac{\lambda_c^3}{2\pi c^2} L \frac{\mathrm{d}^2 n}{\mathrm{d}\lambda^2} \tag{2.2}$$

$$\frac{\mathrm{d}^3\psi}{\mathrm{d}\omega^3} = -\left(\frac{\lambda_c}{2\pi c}\right)^2 \frac{1}{c}\left(3\lambda_c^2 \frac{d^2 n}{d\lambda^2} + \lambda_c^3 \frac{d^3 n}{d\lambda^3}\right) L \tag{2.3}$$

where λ_c is the central wavelength of the laser pulse, ψ is the phase delay, ω is the angular frequency, and L the length of the optical fiber.

In our case, λ_c = 800 nm and L =150 mm. We can then get the amount of GVD arising from the optical fiber. As is seen in the estimated values in Table 2.2, the positive GVD arising from the optical fiber is large, even for the pure silica. In the case of GeO_2 doped silica, the GVD increases with the dopant concentration.

We have considered here the material dispersion arising only from the optical fiber. Actually, there are many other optical elements used in the SNOM system, such as lenses, beam-splitters and mirrors. All of them also yield GVD. These GVD contributions further broaden the pulses and hence degrade the time resolution of the ultrafast SNOM measurements.

2.3 Estimation of GVD generated by a prism pair

Prism pair has been widely used for dispersion compensation since they have the advantage of very low energy loss. Since the refractive index varies with wavelength, the laser beam is dispersed after transmission through the first prism (Fig. 2.2). The short wavelength component is refracted more strongly than the long wavelength component. Therefore, the short wavelength component propagates longer distance through the space between the two prisms than the long wavelength component, while the long wavelength component travels through the prism medium for a longer

distance. This effect introduces a wavelength dependent phase shift, which varies with the distance between the prisms (*l* in Fig. 2.2) and the position of the second prism. We can use a mirror to reflect the beam back so that it passes through the same prisms. This is a folded geometry of the prism sequence compressor [77].

A typical schematic setup of folded geometry of the prism compressor is shown in Figure 2.2. The first prism disperses the beam, while the second prism collimates the dispersed beam.

The GVD introduced by the prism pair is given by,

$$\frac{d^2\psi}{d\omega^2} = \frac{\lambda_c^{\,3}}{2\pi c^2}\left[Ln'' - 4l\cdot(n')^2\right] \tag{2.4}$$

$$\frac{d^3\psi}{d\omega^3} = \frac{\lambda_c^{\,4}}{(2\pi c)^2 c}\left[12l\left(n'^2\left[1 - \lambda_c n'(n^{-3} - 2n)\right] + \lambda_c n'n''\right) - L(3n'' + \lambda_c n''')\right] \tag{2.5}$$

where n is the refractive index of the prism material, $n'(\lambda) = dn/d\lambda$ and $n''(\lambda) = d^2n/d\lambda^2$, λ_c is the central wavelength of light, l is the separation between the prisms, and L is the path-length through the prisms [77].

The first term of Eq. (2.4) is always positive and depends on the path-length through the prisms. The second term is always negative and the value mainly
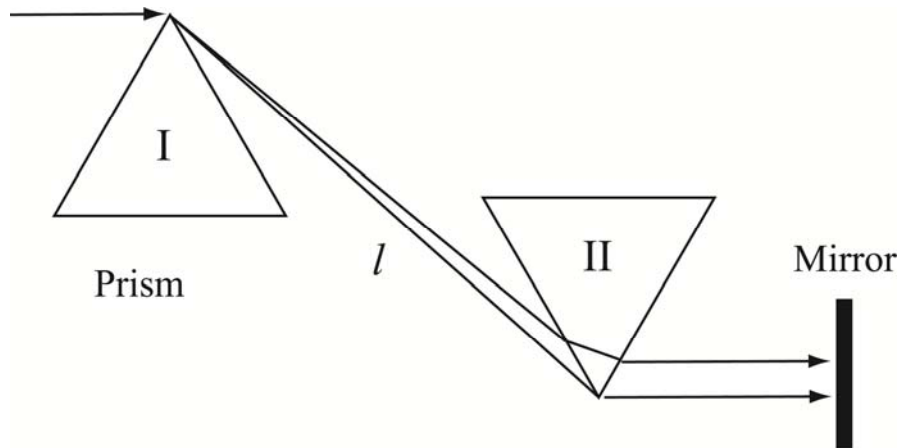

Fig. 2.2 Schematic setup of a prism pair.

depends on the prism separation. By varying the prism separation and the path length through the prisms, we can control the sign and the amount of introduced dispersion. Therefore, in principle, any amount of negative GVD can be generated if large enough prism pair is provided. In practice, however, the size of the prism pair is limited. In the present study, we used two prisms made of SF14 glass and one mirror to make a folded prism compressor, with each prism of 50-mm side length. Since the laser beam width after dispersed by the first prim must be smaller than the side length of the second prism, the separation between the two prisms l is limited to be less than about 700 mm. The dispersion parameters of SF14 glass and the maximum (negative) values of second- and third-order GVD thus calculated with Eqs. (2.4) and (2.5) are summarized in Table 2.3. Since we adopt folded geometry of the prism sequence, the amount of second- and third-order GVD should be doubled. Comparing with the positive GVD arising from optical fiber (see Table 2.2), it suggests that the prism pair can be used to compensate the GVD if the device is large enough.

n	$dn/d\lambda/~10^4$ m^{-1}	$d^2n/d\lambda^2/~10^{12}$ m^{-2}	$d^3n/d\lambda^3~/~10^{18}$ m^{-3}	$d^2\psi/d\omega^2/10^4$ fs^2	$d^3\psi/d\omega^3/~10^4$ fs^3
1.743	-5.5	0.2	-1.1	-0.7672	-0.6214

Table 2.3 Dispersion parameters of SF14 glass and second- and third-order GVD generated by a SF14 prism pair with the separation between the prisms l = 700 mm, at λ_c = 800 nm.

2.4 Estimation of GVD generated by a grating pair

A parallel grating pair could give much larger angular dispersion comparing with that of prism pair. Similar to the prism compressor, it also generates angular

dispersion. The beam of ultrashort laser pulse is incident on the first grating at the blazing angle. The dispersed beam is then incident on the second grating that is
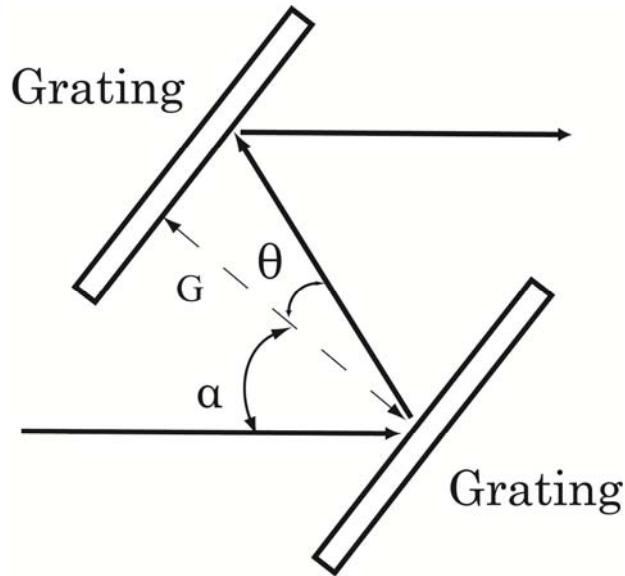

Fig. 2.3 Grating pair that generates negative dispersion.

identical to the first one. The two gratings are arranged fully parallel to each other. Each spectral component of the dispersed beam travels its inherent distance. The higher frequency components arrive earlier than the lower frequency components, resulting in a negative GVD of the grating pair or frequency-dependent phase shift. This concept was first demonstrated by Treacy [67]. He proposed a grating pair as a device that generates negative dispersion as shown in Fig. 2.3.

The equations for calculation of second-order and third-order GVD are given in

groove number / mm^{-1}	d$^2\psi$/dω^2 / 10^4 fs^2	d$^3\psi$/dω^3 / 10^4 fs^3
300	-0.429	0.6
600	-1.62	2.66
800	-2.98	5.73

Table 2.4 Second- and third-order GVD generated by grating pairs with different groove numbers/

Equations (2.6) and (2.7) [77].

$$\frac{d^2\psi}{d\omega^2} = -\frac{\lambda_c}{2\pi c^2}(\frac{\lambda_c}{d})^2\frac{G}{\cos^3\theta} \tag{2.6}$$

$$\frac{d^3\psi}{d\omega^3} = -\frac{3\lambda_c}{2\pi\cos^2\theta}\left[\cos^2\theta + \frac{\lambda_c}{d}(\frac{\lambda_c}{d} + \sin\alpha)\right]\frac{d^2\psi}{d\omega^2} \tag{2.7}$$

where G is the separation between grating surface planes, d is the grating constant (separation between the grooves), λ_c is the central wavelength of the input laser pulse, α is the angle of incidence on the first grating, and θ is the angle between dispersed beam and normal vector of the grating.

If the laser pulse is normally incident on to the first grating and $G = 50$ mm, we obtain the amount of second- and third-order GVD as summarized in Table 2.4.

Comparing with the values in Table 2.2, where the GVD were calculated for an optical fiber, a grating pair may provide negative GVD that is suitable compensate for the positive GVD generated by the fiber if the groove number of the grating is 300 mm^{-1}. If the groove number is 600 or 800, it will give excess negative GVD to compensate for the positive GVD generated by the fiber. From Equation (2.6), the larger separation between two gratings and/or the larger groove numbers of the gratings, the larger negative GVD the grating pair generates.

It is also worth noticed when we compare the GVD for a prism pair and a grating pair (Tables 2.3 and 2.4), that the third-order GVD for a grating pair has an opposite sign to that for a prism pair. This means that, by suitably choosing the device parameters, both second- and third-order GVD generated by an optical fiber can be removed to a certain degree if we combine a grating pair and a prism pair.

To summarize, we can roughly estimate GVD arising from the optical components involved in the system based on the formulae given above. It is important to get rough estimation of suitable device parameters to design the optimized

measurement system.

2.5 Deformable mirror setup

2.5.1 Principle of the deformable mirror

Although prism pair and grating pair have great ability to compensate GVD, a severe problem for these methods is the interdependence of different phase orders, which prevents perfect compensation for arbitrary phase. For example, a grating pair gives negative second-order GVD, meanwhile, it also generates non-negligible positive third-order GVD. This means if we use only a prism pair or a grating pair in the GVD compensation setup, it is hardly possible to remove the entire chirp, and hence it cannot fully recover the pulse duration. The active pulse compression techniques by the use of phase modulation devices such as liquid-crystal modulators (LCM), acoustic-optic modulators (AOM), or deformable mirror (DFM) have a potential to overcome this problem. They have the ability to finely remove the higher-order GVD and have already been widely used in various ultrafast measurements. As for the AOM and LCM, they required an unfolded $4f$ configuration since they are transmissive devices. Additionally, LCM could not provide continuous phase modulation due to the pixilated system, while AOM requires very careful synchronization of the radio-frequency waveform to the laser pulse. In this thesis, the DFM is adopted for the purpose of fine phase adjustments for pulse compression. One of the advantages of the DFM is its smoothly varying phase modulation, in addition to low energy losses (98% reflection). A basic schematic pulse compression setup of a $4f$ system with a DFM is shown in Figure 2.4, where a grating is used to disperse the wave components of laser pulse, and a concave mirror is used to collimate the dispersed beam incident on the DFM

perpendicularly. The grating, concave mirror, and DFM hence make a folded $4f$ system.
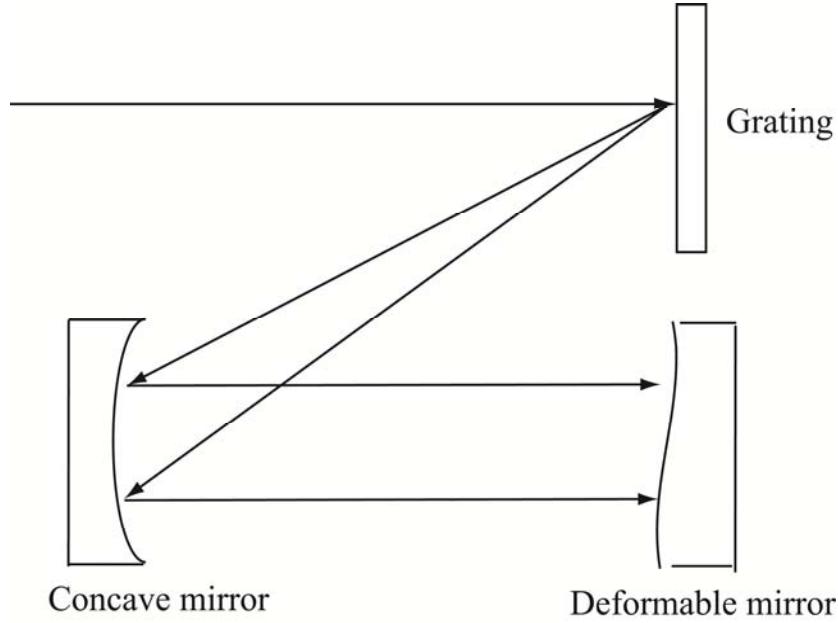

Fig 2.4 Schematic setup of a $4f$ system with a deformable mirror.

The schematic drawing of the assembled DFM and the principle of biased control are illustrated in the Fig. 2.5. The voltage applied to the actuator makes a force to push or pull the mirror, and deforms the surface shape. The surface shape is determined by the combination of all the influence from the actuators. The phase change that the deformable mirror can generate is given in the following equation [72]

$$\phi = 2(2\pi)\Delta z / \lambda_c \qquad (2.8)$$

where Δz is the mirror displacement normal to the surface, λ_c is the central wavelength of the pulse. As an ideal case, we assume that the mirror bend radius is negligible. Since the DFM we adopted is capable to give 9-μm maximum

displacement in the center position, the maximum phase change would be 45π.
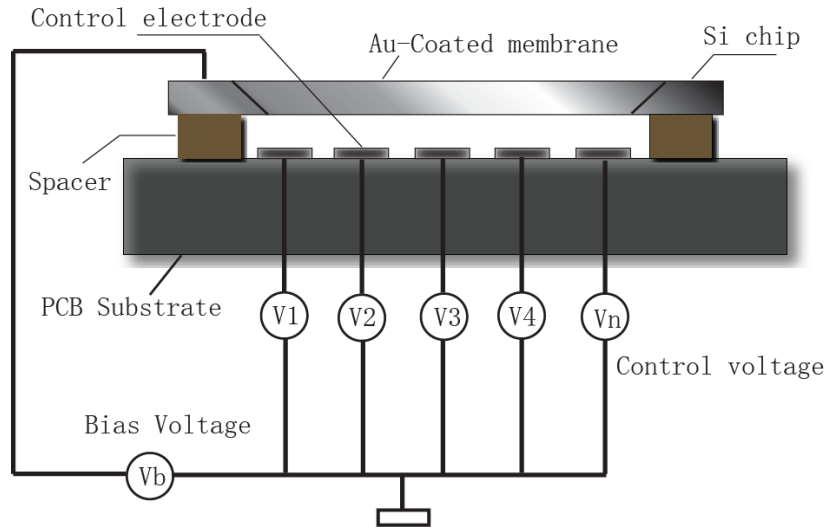

Fig 2.5 Schematic drawing of a deformable mirror. PCB: polychlorinated biphenyl

2.5.2 Genetic algorithm to control the DFM

In order to use the DFM for the pulse compression purpose we have to get a signal that reflects the pulse duration and feed-back control the DFM surface to yield the optimum signal level. For this purpose, second harmonic generation (SHG) signal of the laser pulses is utilized to be optimized. The SHG signal becomes highest when the pulse width is the shortest. Thus the pulse width is optimized by maximizing the SHG signal. To maximize the SHG signal, genetic algorithm (GA) is useful. So a control software for the DFM based upon GA was developed. The GA is a highly efficient and robust search algorithm that simulates evolution in nature [78, 79]. The schematic procedure of the GA in the present study is shown in Figure 2.6.

The basic principle of GA was originally proposed by Holland [78]. It is inspired by the mechanism of evolution by natural selection, where a stronger individual has a greater chance to survive in a competitive environment. In the GA, the candidates of solutions to a problem are regarded as 'individuals' and are parameterized as 'chromosomes'. In each cycle of the evolutionary procedure, a fitter chromosome
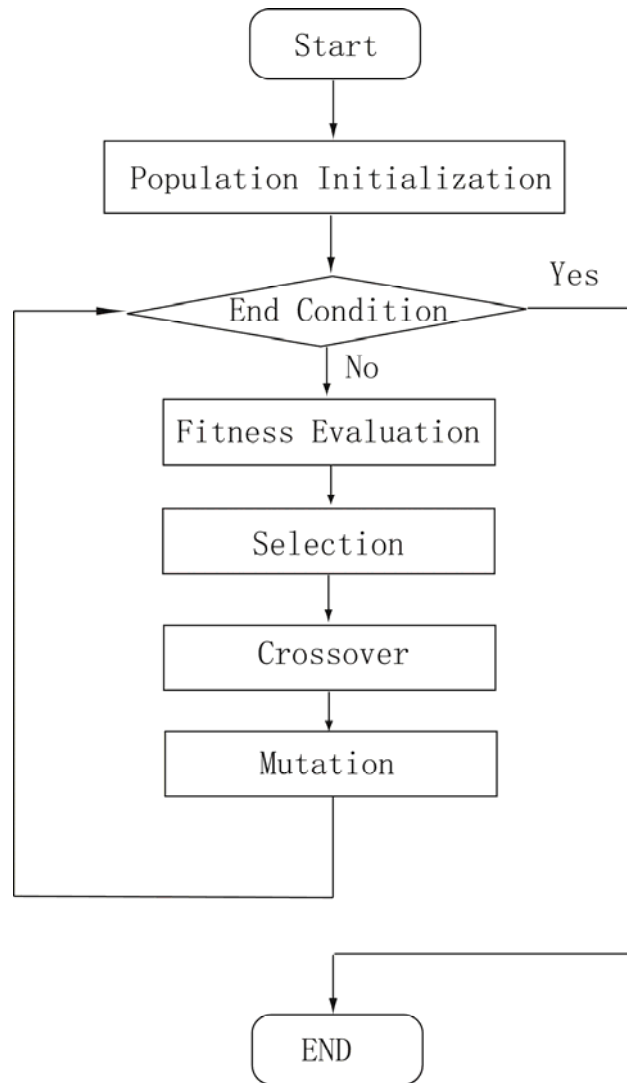
35

Fig. 2.6 Schematic flow of the genetic algorithm adopted.

generates 'offspring' through crossover and mutation. The 'offspring' with better quality is selected and takes the place of their 'parents' through fitness evaluation, which means a better solution to the problem is generated.

In our case, the simplest GA schematically shown in Fig. 2.6 is interpreted as follows.

1.   Initialization of the gene population

Start with a randomly generated population of N 'chromosomes', which are

candidate arrays of voltages (V_k;k=1...N)applied to the element actuators of the DFM. The notes $a_i[0]$ to $a_i[m]$ below denote the voltages applied to the actuators.

V_1 $a_1[0], a_1[1], a_1[2],\cdots\cdots\cdots a_1[m]$

V_2 $a_2[0], a_2[1], a_2[2],\cdots\cdots\cdots a_2[m]$

......

......

......

V_N $a_N[0], a_N[1], a_N[2],\cdots\cdots\cdots a_N[m]$

2. Fitness evaluation

For each chromosome (array of the voltage set V_k applied to the DFM) the SHG signal f_k of the pulses after propagating through the system is collected by the PMT. This signal serves as the fitness parameter for the chromosome V_k. We obtain N fitness parameters ($f_1, f_2, ... , f_N$) for ($V_1, V_2, ... , V_N$)when this step is finished.

3. Selection

In the present case, a roulette wheel approach is adopted as the selection procedure of the chromosomes. These voltage arrays V_k yielding higher SHG intensity have more chances to be selected, while the other ones is abandoned. The roulette wheel procedure is progressed as described below:

- Step1: Sum up the SHG intensity of all voltage arrays, $F = \Sigma f_k$

- Step2: Calculate selection probability p_k for each voltage array V_k as $p_k = f_k/F$

- Step3: Calculate cumulative probability $q_k = p_1+p_2+ ... +p_k$ for each voltage array V_k

- Step4: Generate a random number r within the range of [0,1]

- Step5: If $r \leq q_1$, then select the first array V_1; otherwise, select the k-th

array V_k ($k = 2, 3, ..., N$) such that $q_{k-1} < r \leq q_k$

4. Crossover

This operator exchanges some voltage values of two voltage arrays (i.e., chromosomes) to create two chromosomes of offspring, with a probability varying from 0 and 1. For example, the voltage arrays of the first two chromosomes:

$$V_1 \qquad a_1[0], a_1[1], a_1[2], \cdots\cdots\cdots\cdots a_1[m] \qquad \text{and}$$

$$V_2 \qquad a_2[0], a_2[1], a_2[2], \cdots\cdots\cdots\cdots a_2[m]$$

are crossed over by exchanging the first two voltages, and in this case the new chromosomes of offspring are:

$$V_1 \qquad a_2[0], a_2[1], a_1[2], \cdots\cdots\cdots\cdots a_1[m] \qquad \text{and}$$

$$V_2 \qquad a_1[0], a_1[1], a_2[2], \cdots\cdots\cdots\cdots a_2[m]$$

This operator roughly mimics biological recombination between two single-chromosome organisms. If no crossover takes place, it generates two individuals that are the exact copies of their respective parents.

5. Mutation

This operator changes some voltage(s) in a voltage array (chromosome) with a probability ranging from 0 to 1. For example, the value of $a_1[2]$ in V_1 is changed with a randomly chosen value in the mutation:

$$V_1 \qquad a_1[0], a_1[1], a_1'[2], \cdots\cdots\cdots\cdots a_1[m]$$

6. End condition.

If the highest SHG signal is obtained, which means the best solution (fittest to the problem) is found, or it reaches the pre-set maximum iterative number, then the process of the algorithm terminates.

Chapter 3

Basic performance of pulse compression devices combined with fiber-probe SNOM

In this chapter we examine the basic performance of the pulse compression system, for a few of combinations of GVD compensation devices (prism pair, grating pair, and $4f$ optical system with DFM). The width of ultrashort optical pulses are measured after propagating the pulse compression system and the optical fiber, based mainly upon interferometric (fringe-resolved) autocorrelation measurements.

3.1 Combination of prism pair and DFM

In Chapter 2 we tried to calculate GVD for the optical fiber and the GVD compensation devices. The results show that the combination of prism pair and deformable mirror might give enough negative GVD to compensate the positive GVD arising from the optical components. Therefore, we first launched the experiment to check the performance of this GVD compensator with the setup shown in Fig. 3.1. This is a far-field measurement of the pulse duration (the near-field microscope is not installed), since it is advantageous for checking performance due to easier alignment and much simpler experimental configuration comparing with the near-field measurement. It still provides useful information on the performance of the compensator, however.

In this setup, the laser pulse centered at 800 nm (~15 fs pulse duration) was incident on a reflection type grating (600 grooves/mm), and the dispersed light was collimated by a concave mirror to incident on the DFM. These optical elements form a $4f$ system. The DFM was a product of OKO Technologies, based on the technology of silicon bulk micromachining. The device consists of a silicon membrane mounted over a printed circuit board holder. The membrane (11 mm x 39 mm) is coated by a gold film and suspended over an array of 19 actuator electrodes on a printed circuit board. The 19 actuators are arranged linearly below the membrane. The maximum
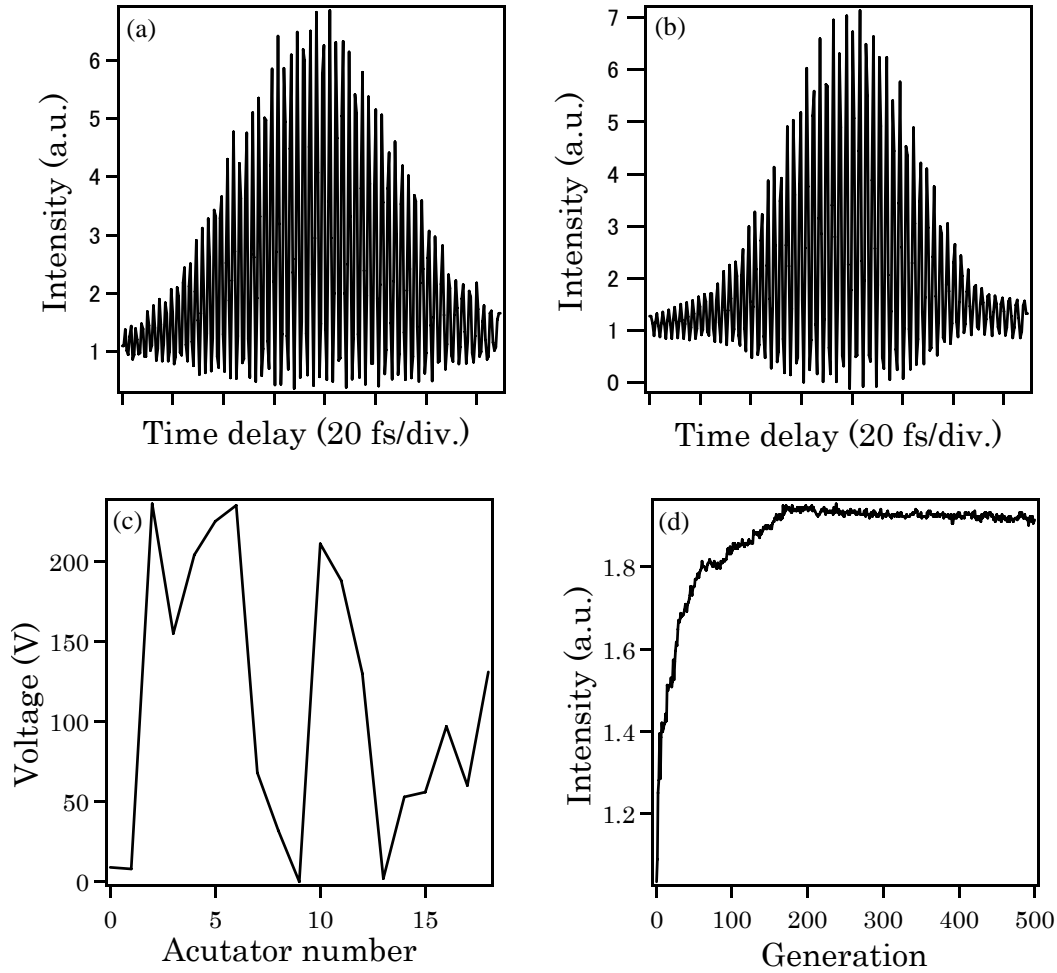
Fig 3.1 Schematic experimental setup for the far-field autocorrelation measurement with a prism pair.

displacement of the mirror surface in the center position of the mirror is 9 μm. The reflected-back beam was then picked out and sent to the SF14 prism pair. The apex angle of each prism is equal to the Brewster angle at a wavelength of 800 nm. The prisms were arranged in such a way that the beam entered in and exited from each prism at the Brewster angle. The laser beam was then coupled into a 150-mm long optical fiber. At the other end of the fiber, another objective lens was used to collimate the optical output from the fiber. The beam was separated into two parts after the fiber and the lens. One was incident on an autocorrelator for the far-field autocorrelation measurement, and the other was focused onto a 100-μm BBO crystal to generate the feed-back signal for the DFM control. The generated SHG radiation was detected by a PMT and the signal was sent to the computer as the parameter for the GA. The distance between the two prisms was set to be ~700 mm in order to get as large as possible negative GVD, which was the maximum separation in the present experimental setup.

42

Fig.3.2 (a) Autocorrelation trace before optimiazation of DFM. (b) Autocorrelation trace after optimiazation of DFM. (c) The voltage applied to each actuator of the DFM after optimization. (d) The intensity of the SHG signal as a function of the generation.

Fig 3.2a shows the autocorrelation trace measured before the optimization process of the DFM at a position after the optical fiber. The FWHM of the trace is ~83 fs, which corresponds to the pulse duration of about 55 fs. The peak-to-background ratio is about 7. Fig 3.2b shows the autocorrelation trace after the optimization of the DFM to maximize the SHG intensity. The optimization procedure was finished (i.e., the SHG intensity reached its maximum) within 200 generations in ~5 minutes, as shown in Fig 3.2d. The FWHM of the autocorrelation trace is reduced to about 67 fs, which corresponds to the pulse duration of about 44 fs. However, the

43

peak-to-background ratio is still about 7. The pulse duration after optimization of the DFM did not change much, and was still far from the original pulse duration of the laser output (~15 fs). It indicates that serious GVD remained.

The separation between two prisms is a key parameter that determines the amount of negative GVD. As we discussed in Chapter 2.3, the prism material itself also generates positive GVD. If the separation is not enough, it does not have an ability to compensate the positive GVD due to the fiber. It may even add additional positive GVD to the laser pulse. The maximum second-order negative GVD that could be generated by the SF14 prism pair is -15344 fs^2, while the positive GVD generated by a 150 mm optical fiber (19.3% GeO_2 doped) is 7655.05 fs^2, as shown in the calculation of the previous Chapter. From this estimation, we may expect that the positive GVD due to the optical fiber may be compensated by the negative GVD introduced by the prism pair. The reality is, however, the original pulse width was not recovered at the position after the fiber even after the optimization of the DFM. The situation was not improved even when the prism distance was shortened. The origin of this unfavorable result has not been clear yet, but there may be a few of possible reasons. It may partially be due to other optical components in the system such as lenses and mirrors and difficulties in precise alignments of the setup. It may be also conceivable that the GVD of the fiber is actually larger than that estimated. The negative second-order GVD produced by the prism pair is possibly not as high as calculated because, for example, the beam practically have to travel through the glass longer than the ideal case due to the finite beam size. As for higher-order GVD, although the signs of second- and third-order GVD by the prism pair device estimated in Chapter 2 (-15344 fs^2 and -13428 fs^3, respectively) are both opposite to the corresponding ones generated by the fiber (7655 fs^2 and 3352 fs^3 for 19.3% GeO_2), the respective magnitudes do not match quantitatively. This fact may also affect the

44

performance of the GVD compensation system.

Fig. 3.2c shows the voltage applied to each actuator of the DFM after the optimization process. The horizontal axis corresponds to the lateral position on the DFM surface. Since the voltages applied to the actuators determine the displacements normal to the surface of the mirror, they may give us a qualitative measure of the surface shape of the DFM. From the surface shape, we can judge roughly whether the GVD has been removed. If the voltage curve is smooth enough (= surface shape is smooth) and the applied voltages are within a relatively small range, it shows that the GVD has been in most part removed. If the curve is not smooth and/or the voltage amplitude is close to the maximum applicable voltage of the DFM (~250 V), it means the GVD is too much to compensate for with the GVD compensator. In Fig. 3.2c it is clear that the voltage applied to some of actuators were saturated. This observation shows that the prism pair and the DFM are not sufficient to remove all the GVD generated from the optical fiber and other optical elements.

3.2 Combination of grating pair and DFM

The combination of prism pair and the DFM could not provide enough negative GVD for the full compensation of GVD due to the fiber and other optics. We thus tried another type of GVD compensator, which consists of a grating pair and the DFM. The experimental setup for the measurement is shown in Fig. 3.3. In this setup the autocorrelation measurement was performed in the near-field regime. The output from the laser source with a pulse width of ~15 fs was split into two parts, with the intensity ratio of 1:1. In one arm of the optical-delay setup a piezo-stage

with a maximum movement of 20 µm was installed to precisely adjust the mirror position. The beam splitter was self-designed to balance the dispersion effects in both arms of the optical delay lines. As Fig. 3.4 shows, each side of the beam splitter was reflection coated with dielectric materials for its half area, while the other half part was kept bare. With this configuration, the optical length through the substrate material for each arm was completely the same, resulted in the same amount of GVD. This beam splitter was also adopted in the time-resolved experiments of the samples. After the optical delay stage, the two beams were fully overlapped and sent to the 4*f* system. The beam was dispersed by a gold-coated grating (600 grooves/mm), incident on a concave mirror, and then the collimated beam was incident on the DFM. The reflected back beam was then picked out and incident on a grating pair.
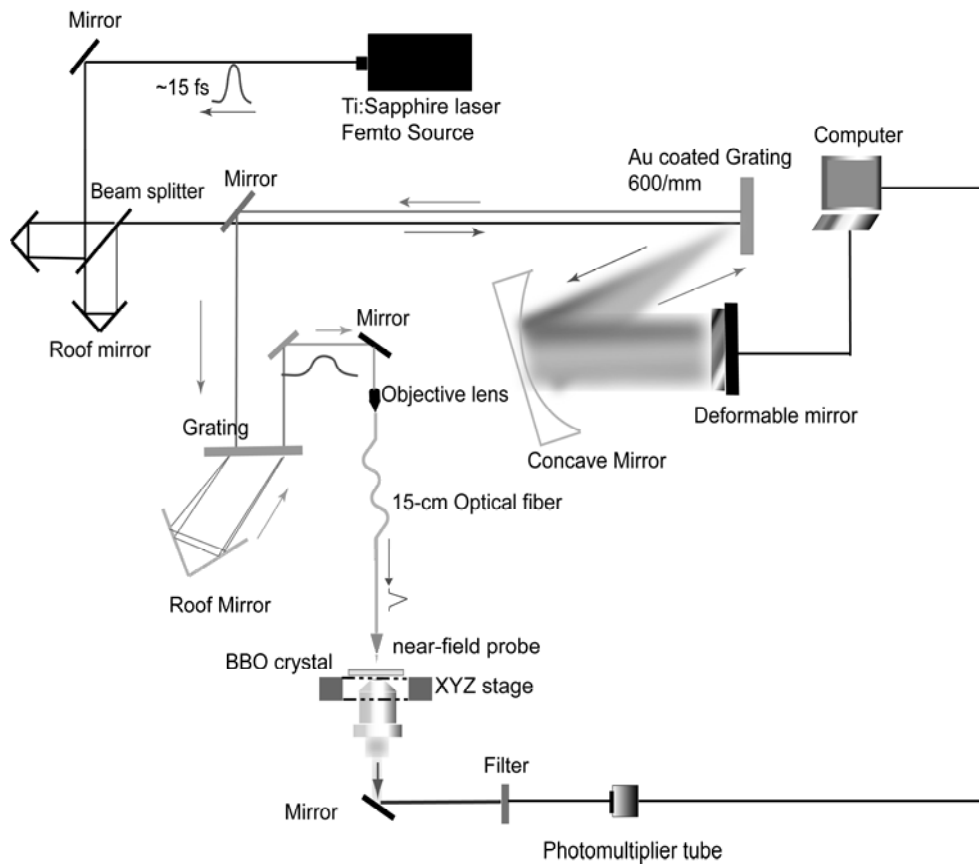
Fig. 3.3 Schematic experimental setup for the near-field autocorrelation measurement, with a grating pair.

Practically, a transmission-type grating and a roof mirror as arranged as an equivalent of a grating pair for the easiness of alignment, which is essentially the same as a reflection-type grating pair. The groove number of the grating was 300 mm^{-1}, which is a compromise of the GVD compensation ability and the practical geometrical configuration. A gold-film coated roof mirror was used to reflect back the beam in laterally correct direction. The beam was then coupled into a 150-mm long optical fiber, at the other end of which a near-field aperture probe tip was fabricated. The laser pulse emanating from the probe aperture irradiated a 100-μm BBO crystal. The generated SHG signal was collected by a microscope objective and detected by a PMT, and the signal was sent to the computer as a feed-back signal to be optimized in the GA. After optimization of DFM the autocorrelation was recorded by plotting
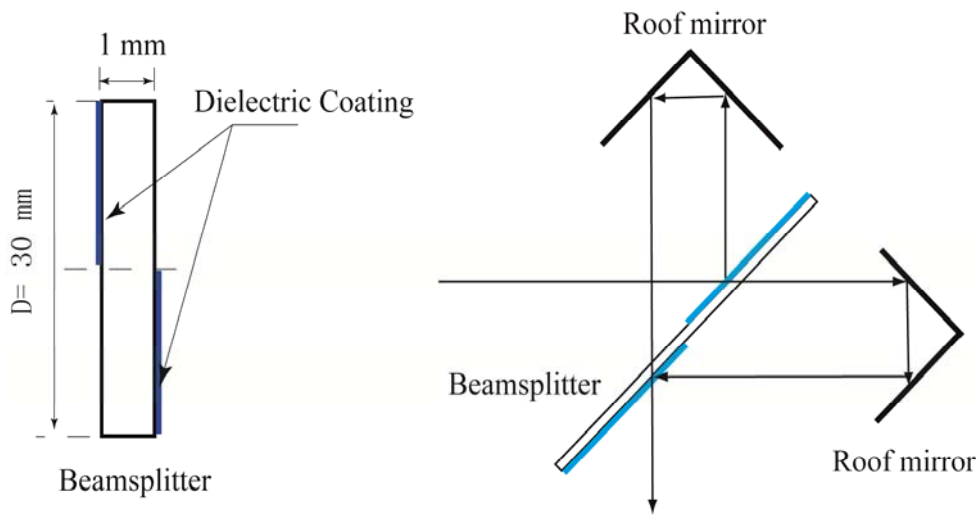
Fig 3.4 Schematic design of the beam splitter and the optical delay setup.

the intensity of the SHG signal against the position of the optical delay stage.

Fig 3.5a shows the auotocorrelation trace of the pulses in the near-field regime before the optimization of the DFM. The FWHM of the trace is about 75 fs, which corresponds to a ~50 fs pulse duration. The peak-to-background ratio is about 4:1, which is far from the value of transform-limited pulses, 8:1. Fig. 3.5b shows the autocorrelation trace after the optimization of the DFM. The optimization procedure was finished within 100 generations as shown in Fig. 3.5d. The FWHM of the trace is about 29 fs, which corresponds to ~18 fs pulse duration. It indicates the pulse duration was greatly reduced after optimization process of DFM.

The peak-to-background ratio is nearly to 7. However, there is still non-negligible side wings remained, and the pulse duration of ~18 fs is a little longer than the original pulse at the direct output of the laser (~15 fs). Fig. 3.5c shows the voltages applied to the actuators of the DFM after the optimization. It clearly shows that the voltages were still nearly saturated (>200 V) for some actuators. This result indicates that the GVD compensator was not effective to fully compensate the GVD
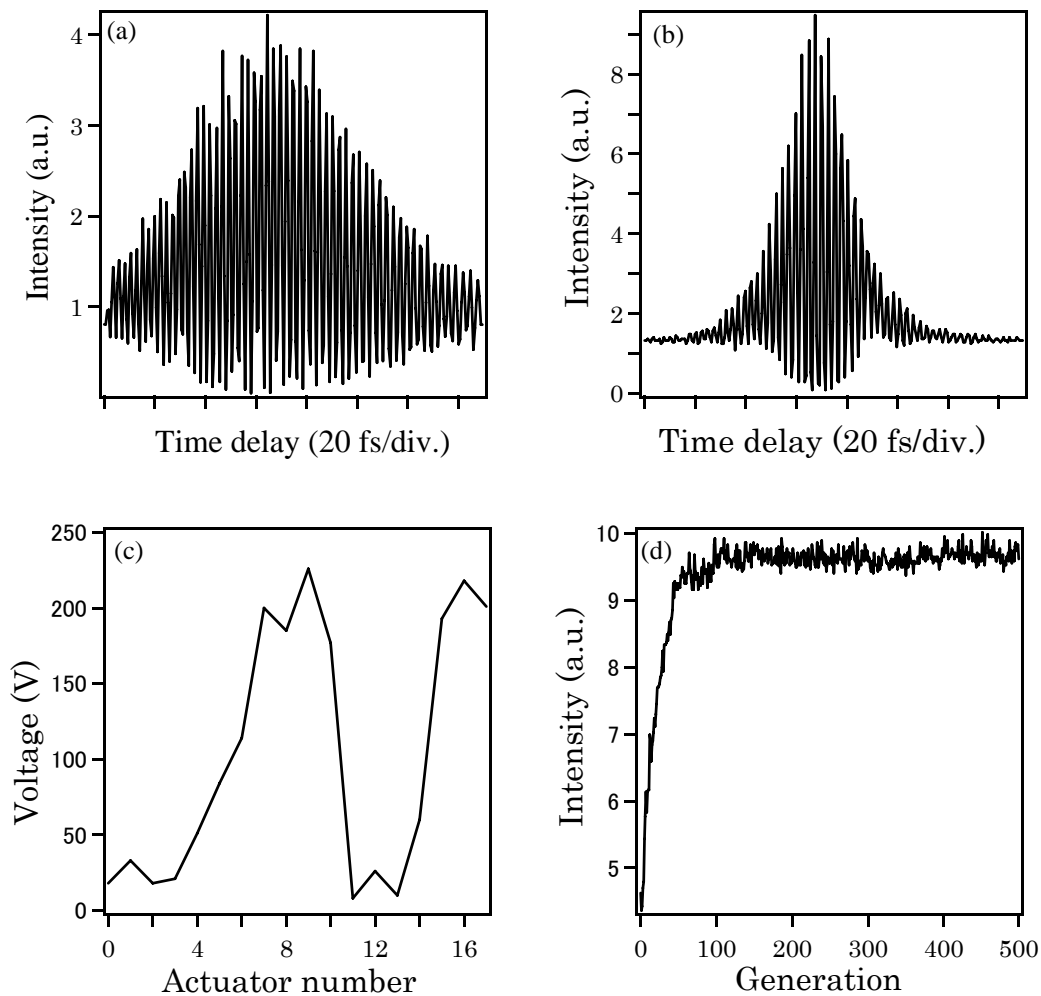
Fig. 3.5 (a) Autocorrelation trace for the pulses at the probe tip before optimization of DFM. (b) Autocorrelation trace for the pulses at the probe tip after optimization of DFM. (c) The voltage applied to each actuator of the DFM after optimization. (d) The intensity of the SHG signal as a function of generation.

arising from the fiber and other optics. As estimated in Chapter 2, the second order GVD produced by the grating pair (-4290 fs^2 for a 300 mm^{-1} grating and 50-mm

grating separation) must be sufficiently high to compensate for that arising from the fiber (7655 fs^2 for 19.3% GeO_2 doped) if the grating separation is suitably adjusted.

Then, one of possible reasons for the finding mentioned above is higher-order GVD due to the fiber as well as the grating pair device. The third-order GVD arising from the fiber is estimated to be positive (3352 fs^3 for 19.3% GeO_2) and that from the grating pair is also positive (6000 fs^3 for 300 mm^{-1} grating with 50 mm separation). This means that the grating pair can never compensate for the third-order GVD, or the device gives even worse effects in view of third-order dispersion. The major reason for the remaining GVD in the present case is therefore considered to be the third-order GVD, and the use of the combination of both grating pair and prism pair may be effective to fully compensate the GVD arising from the fiber, which is the subject of the next Section.

3.3 Combination of prism pair, grating pair, and DFM

As mentioned in the previous section, both the prism pair - DFM setup and grating pair - DFM setup could not fully remove the GVD arising from the fiber and the optical elements. This result was considered to be partially arising from higher order (especially third order) GVD. While the grating pair gives positive third-order GVD, the prism pair may provide negative third order GVD. Then the combination of the prism pair and the grating pair may be effective to pre-compensate both second- and third-order GVD. We try in this Section combination of both the prism pair and the grating pair with the DFM to remove GVD and recover the original pulse width of the laser at the probe tip.

The layout of the experimental setup is shown in Fig. 3.6. The laser pulse from a Ti:sapphire laser (~15 fs, 800 nm, 80 MHz) was split into two parts with an intensity ratio of 1:1. The two beams were completely overlapped after the optical delay setup and then the combined beam was sent to an SF14 prism pair and a pair of transmission gratings (600 grooves/mm)，the pulse is further dispersed by a grating (300 grooves/mm) and focused by a concave mirror (f = 400 mm) onto a deformable mirror ($4f$ system). We adopted here the transmission grating instead of reflection type grating because the optical alignment becomes much easier. The positive GVD introduced by the glass of the grating itself can be canceled by appropriately adjusting the GVD compensation devices. The $4f$ system, the grating pair, and the
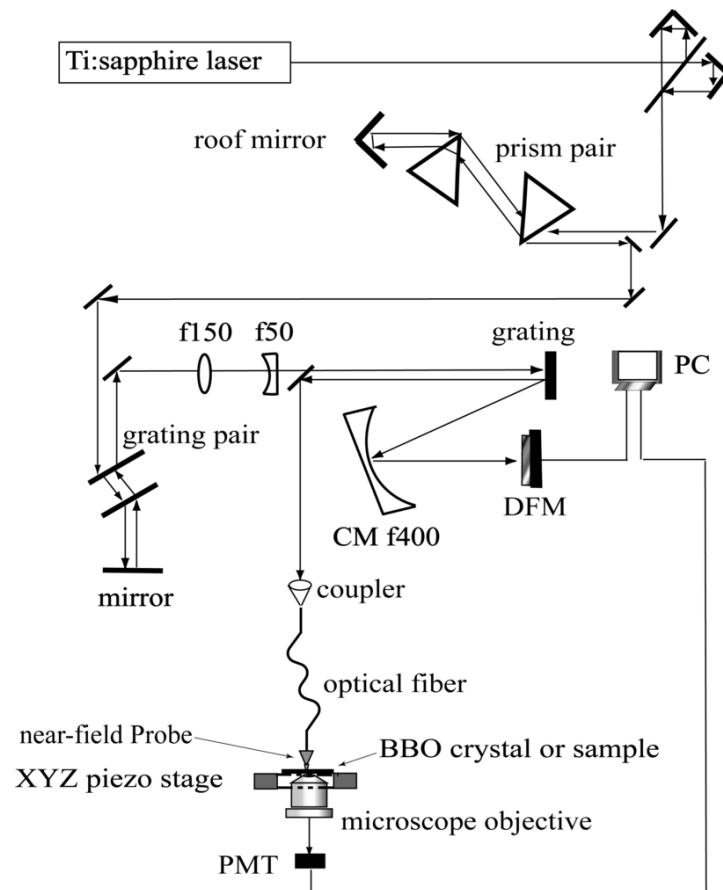
Fig. 3.6 Schematic experimental setup for the near-field auotocorrelation measurement with the GVD compensator consists of prism pair, grating pair, and DFM.

prism pair act as a pulse shaping system that compensates GVD arising from the optical fiber and other components. The laser beam was then coupled to the cleaved end of a 150-mm long optical fiber to introduce the light into the apertured near-field probe tip. To get an autocorrelation trace of the pulses in the near-field regime, a 100-μm thick BBO crystal was set immediately after the probe tip. The SHG signal was collected by the microscope objective and detected by a PMT, and recorded as a function of the delay time between the two pulses. The SHG signal at a fixed delay time was used as a signal to optimize the surface shape of the DFM.

Figure 3.7a shows a typical far-field autocorrelation trace for the direct output from the Ti:sapphire laser using a conventional autocorrelator. The FWHM is ~25 fs,
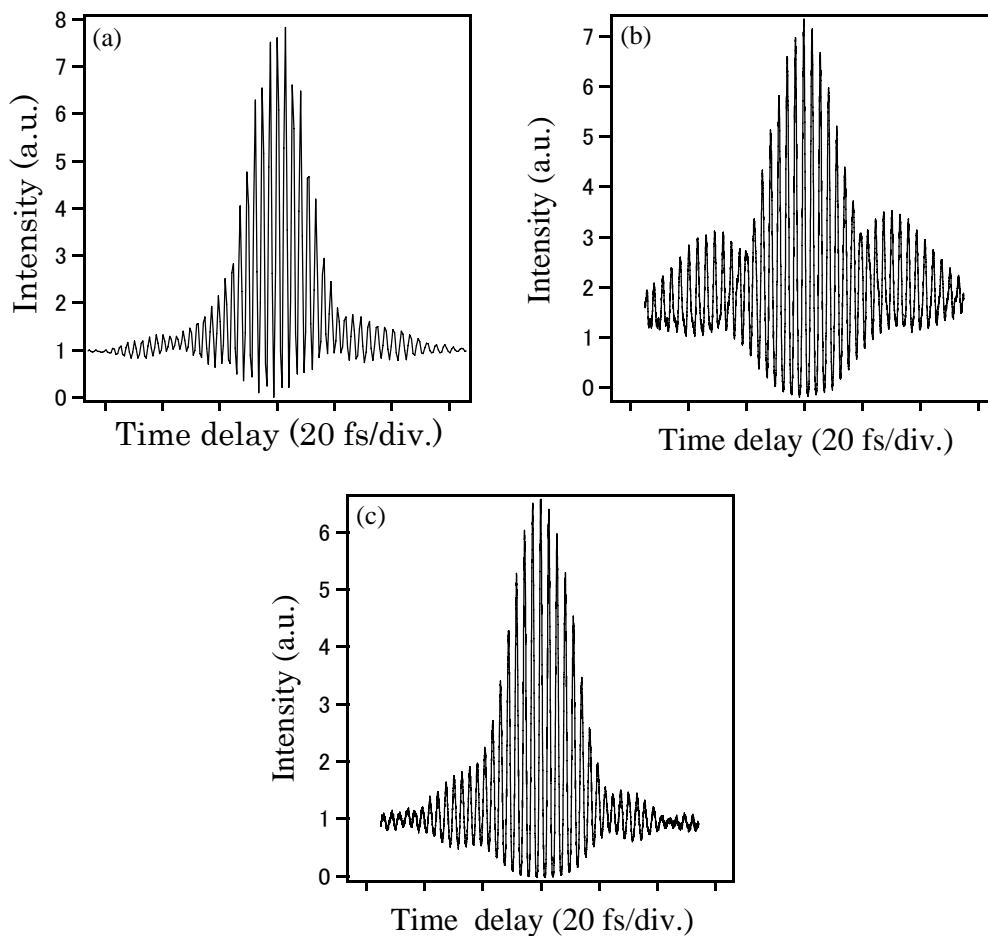
Fig.3.7 (a) Autocorrelation trace measured for the direct output from the Ti:Sapphire laser. (b) Autocorrelation trace at the probe tip before optimization of the DFM. (c) Autocorrelation trace at the probe tip after optimization of the DFM. (to be continued)

52

corresponding to a pulse duration of ~16 fs if we assume a sech² pulse shape. Figure 3.6f shows a spectrum measured for the pulses at the same position. The half-width of the spectrum is ~73 nm, which gives a time bandwidth product of ~0.56 compared with 0.315 for transform-limited sech² pulses. The discrepancy may partly arise from the effects of the dispersive optics involved in the autocorrelator, such as a beam splitter.

The situation is similar for the near-field measurements described below. Fig 3.7b shows a typical autocorrelation trace for the pulses after propagated through a
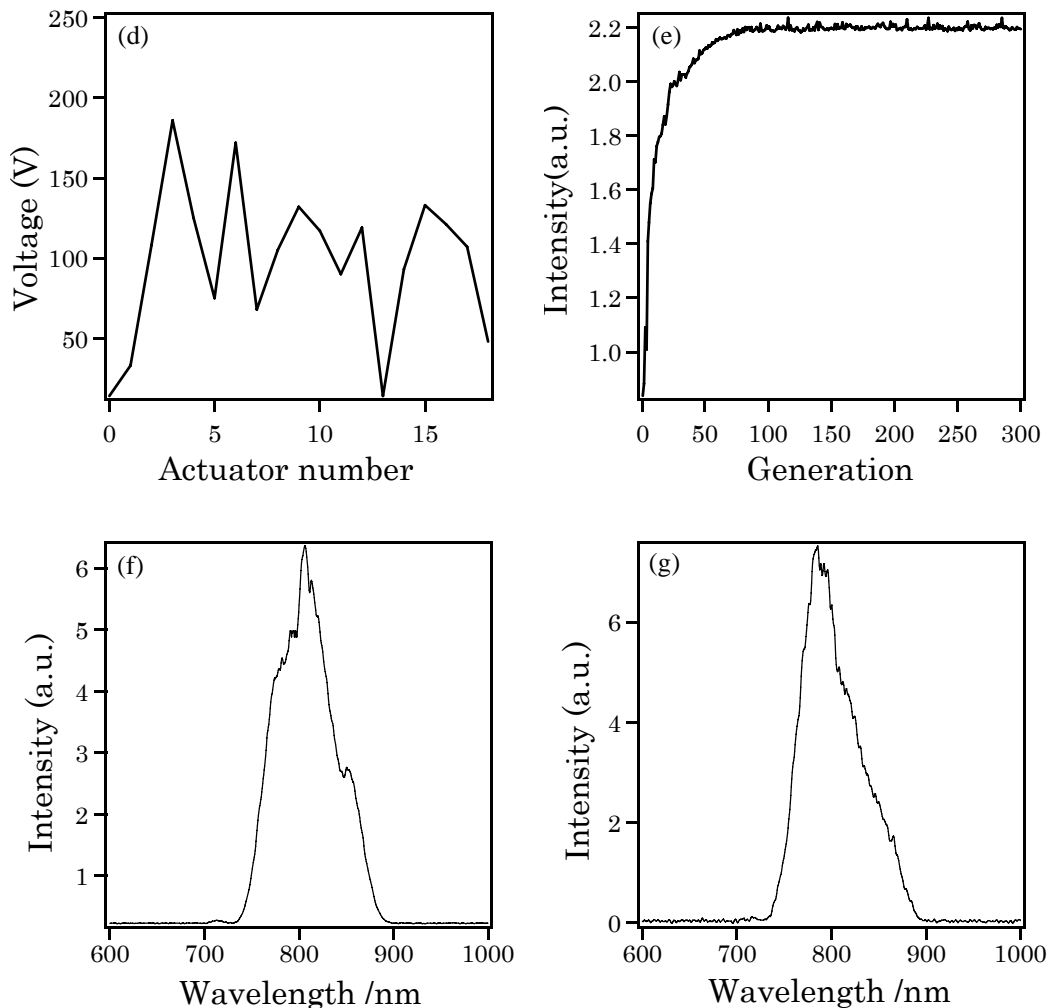
Fig. 3.7 (continued) (d) The voltage applied to each actuator of the DFM after the optimization. (e) The intensity of the SHG signal as a function of generation. (f) Spectrum of the laser radiation measured for the direct output of Ti:sapphire laser. (g) Spectrum of the laser radiation measured behind the sample position.

150-mm optical fiber before optimization of the DFM, which is obtained in the near-field regime. The grating pair and the prism pair were adjusted to give the shortest pulse width. The autocorrelation width is much broader than that of the output from the laser, although the prism pair and the grating pair were nearly optimized. The pulse shape is obviously distorted from that of the transform-limited pulses, and the intensity ratio of the peak at the center to the background (~3.5:1) is much lower than that of the ideal transform-limited cases (8:1). This is probably because the effects of GVD arising from the optical fiber were not fully compensated by the grating pair and the prism pair, which remove the major part of the second- and third-order dispersions.

The result after optimization of the surface of the DFM is shown in Fig. 3.7c. The optimization procedure was finished within 100 generations as shown in Fig. 3.7e. The autocorrelation half-width is ~26 fs, which corresponds to pulse duration of ~17 fs. The pulse duration is nearly equal to that of the laser source. The peak to background intensity ratio is much closer to 8:1. Figure 3.7g shows the spectrum of the radiation after the near-field aperture measured at a position behind the BBO crystal (i.e., far-field spectrum behind the tip). The spectral width is ~63 nm. The narrower spectral width compared with the direct laser output may arise mainly from partial loss of spectral components at the entrance into the optical fiber. Because the total optical path is relatively long (>3 m), the dispersive optical components can cause slight angular dispersion for each spectral component. This results in partial loss of the spectral components at the incidence into the fiber. If we assume that the spectrum measured behind the BBO crystal is nearly the same as that at the tip, the time-bandwidth product in the near-field regime is estimated to be ~0.50. It shows that the GVD was almost fully removed after optimization of the DFM. This is consistent with the peak to background ratio of nearly 8:1 in the

54

autocorrelation trace in Fig. 3.7c. The voltages applied to the actuators of the DFM are less than 200 V for all the actuators (Fig. 3.7d), which suggests that the higher-order GVD was also effectively removed by this compensator system. In summary, it has been shown in this Chapter that the combination of both the prism pair and the grating pair with the DFM device gave a sufficient performance to fully recover the original pulse of ~15 fs at the near-field probe tip.

Chapter 4

Measurement of dephasing of SPR in gold nanostructures by ultrafast SNOM

As described in the previous Chapters, we have succeeded in delivering ultrashort optical pulses as short as ~17 fs to the near-field probe tip in SNOM, with a <100-nm spatial resolution. In this Chapter, we try time-correlated two-photon induced photoluminescence (TPI-PL) measurements for a gold nanoparticle to investigate the dephasing time of SPR. The principle of the measurement with TPI-PL has been described in Section 1.3.2. The basic experimental setup is the same as that in Fig. 3.5. The BBO crystal was replaced with the gold nanoparticle sample. The light pulses were incident on the sample through the near-field probe to excite the TPI-PL from gold. The photon emission in the wavelength region <720 nm was detected and the intensity was recorded as a function of the delay time between the two pulses.

The gold nanostructure samples were prepared by electron-beam (EB) lithography method. Figure 4.1(a) shows the field-emission scanning electron micrograph (FE-SEM) of the sample. The sample was a gold nanoparticle dimer array. Each nano-dimer consisted of two elliptically shaped nanoparticles, with a size of $110 \times 90 \times 20$ nm^3. The SEM measurement shows that the EB-lithography prepared gold nanoparticles were in a nearly homogenous size and shape. Comparing with the
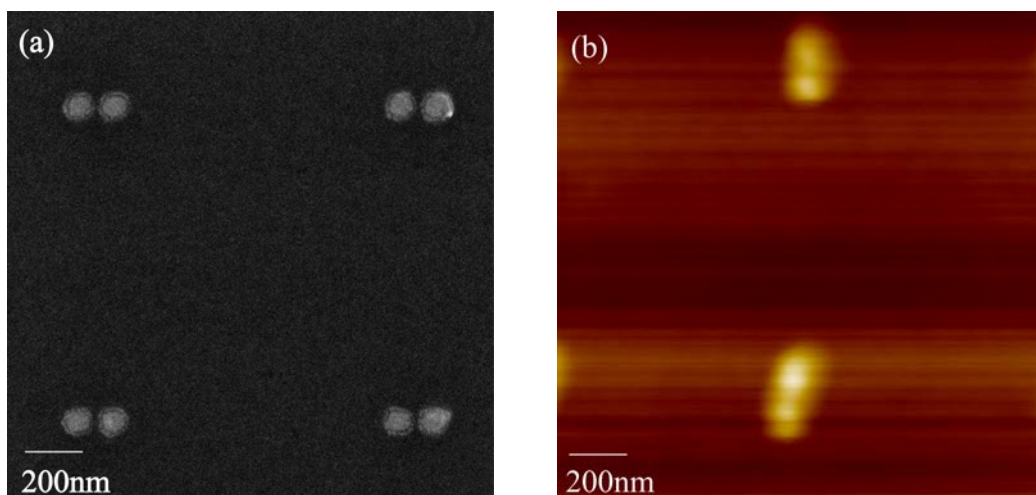
Fig. 4.1 (a) FE-SEM and (b) AFM images of the gold nano-dimer array sample.

chemically synthesized gold nanopartiles, the EB lithography prepared gold nanoparticles are tightly adhered on the glass substrate. These characteristics are advantageous for the SNOM measurements, since the probe tip may drag the particles and change their positions during the scanning procedure. Figure 4.1(b) shows the topography measured by the AFM. Figure 4.2(a) shows the topography measured by the SNOM system, and Fig. 4.2(b) the cross-section profile of the sample along the line indicated in Fig. 4.2(a). From both the AFM and SNOM topographies the height of the gold nanoparticles was estimated to be in the range of 12 to 20 nm.

Now we measure the dephasing of SPR in the time domain at a local position on a particle by the ultrafast SNOM. We first measured the SHG autocorrelation trace with the BBO crystal beneath the near-field probe as described in the previous Chapter, to get the system response function.. The result is shown in Fig. 4.3(a). The FWHM of the trace is ~26 fs as described in Section 3.3. Then, the BBO crystal was replaced with gold nanoparticle sample to perform the time-correlated TPI-PL
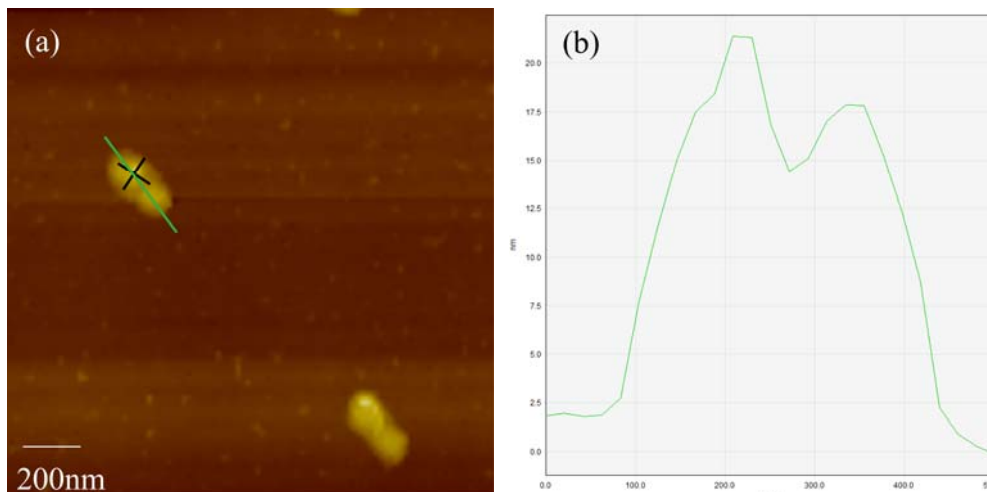
Fig. 4.2 (a) SNOM topography image of the gold dimer. (b) Cross-section profile of the gold nanoparticle dimer measured at the solid line in (a). The mark x indicates the position of the time-correlated TPI-PL measurement in Fig. 4.3(b).

measurement. Since the optical alignment for the sample measurement is exactly the same as that for the autocorrealtion measurement by using the BBO crystal, the autocorrelation gives the exact system response function of the measurement.

The time-correlated TPI-PL measurement was performed at the position marked with × indicated in Fig. 4.2(a), which is near the center of a gold nanoparticle. The obtained time-correlated TPI-PL signal is shown in Fig. 4.3(b). Compared with the autocorrelation trace of the pulses in Fig. 4.3(a), the width of the time-correlated TPI-PL signal profile has been found broader than that of the SHG auotocorrelation
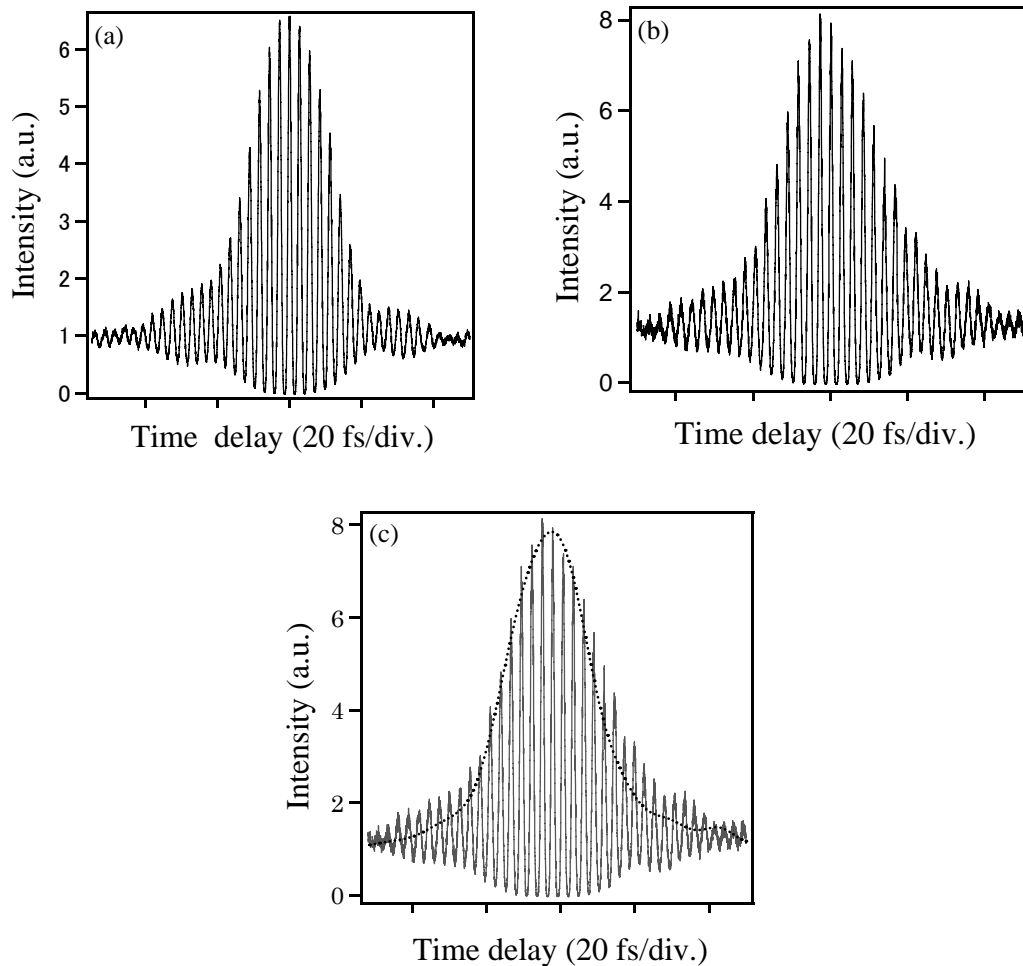
Fig. 4.3 (a) The interferometric SHG autocorrelation trace at the near-field probe tip measured with the BBO crystal. (b) The time-correlated TPI-PL trace measured for the gold nanoparticle shown in Fig. 4.2(a). (c) Comparison of the time-correlated TPI-PL trace (solid curve) with the autocorrelation envelope trace extracted from the data in Fig. 4.3(a) (dotted curve).
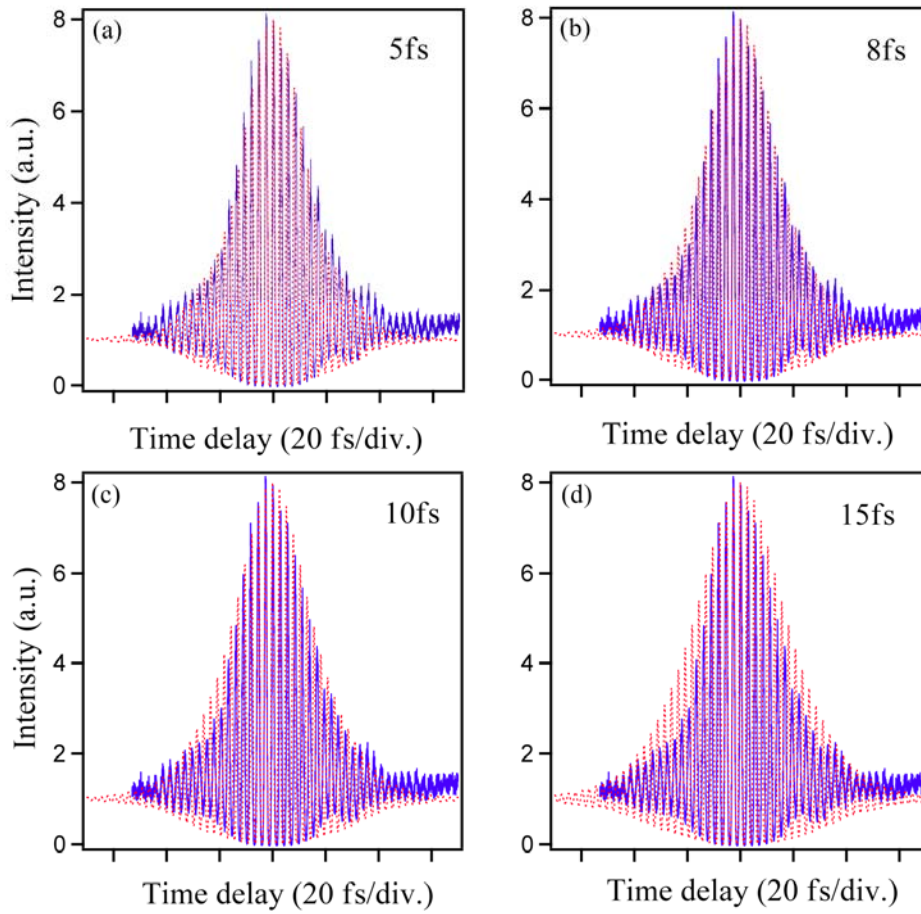
Fig. 4.4 The time-correlated TPI-PL trace for the gold nanoparticle (same as Fig. 3.2 (b), solid blue curves) and the simulated curves assuming the dephasing times of (a) 5 fs, (b) 8 fs, (c) 10 fs, and (d) 15 fs (dotted red curves).

trace, with a sufficient repeatability. In Fig. 4.3(c), the envelope of the SHG autocorrelation is plotted together with the time-correlated TPI-PL trace, to directly compare them in detail. (The envelope was extracted by removing the high-frequency components from the autocorrelation trace.) The broadening is attributed to the finite dephasing time of the plasmon resonance in the gold nanoparticle.

In order to estimate the dephasing time quantitatively, we performed simulation of the time-correlated TPI-PL trace in Fig. 4.3(b), based on the simulation model described in Section 1.4.2. Comparison between the observed trace and the

simulated traces assuming the dephasing times of 5, 8, 10, and 15 fs are summarized in Fig. 4.4. We find that the best-fit curve has been obtained when the dephasing time is set to be 8 fs. In the case of 5 and 10 fs of the dephasing times, the widths of the simulated curves are slightly but definitely narrower and wider, respectively. From these results we conclude now that the dephasing time of the nanoparticle was 8±3 fs. This indicates that our ultrafast SNOM system has a capability to resolve ~10 fs decay in time domain measurements while maintaining a spatial resolution of 50-100 nm.

According to the previous study [58] based on the band-width analysis of the light-scattering spectra, the SPR dephasing times of chemically synthesized gold nanorods were found to be 6 to 18 fs depending on their dimensions. The reported value is in good agreement with the present result obtained in the near-field ultrafast measurement. Since the dephasing time is affected by the surface scattering, spatially resolved dephasing measurements for single nanostructures in the near future may yield fundamental information on the decay mechanism.

Comparing with the dephasing time of nanospheres on glass substrates in the air (1-5 fs) [58], the dephasing time of the gold nanoparticle obtained in our measurement is a little longer. This is probably because our nanoparticle was rod-shaped. Sönnichsen et al. found that the interband damping in the nanorods was reduced because of a decreased spectral overlap between the longitudinal plasmon resonance at lower energies and the interband transition. They further concluded that the pure dephasing T_2^* is negiligble and the plasmon dephasing time T_2 is mainly dominated by T_1. Therefore, the 8 fs dephasing time for our nanoparticlels may be mainly contributed by the inelastic process [80].

For spherical metal nanoparticles, the dephasing time of SP, T_2, and the local field enhancement factor, f, are roughly related to each other as $f \propto T_2$. This means that

the longer dephasing time yields stronger field enhancement. The enhancement factor of the optical field in the vicinity of the nanoparticle hence may be closely related to the obtained dephasing time. In surface enhanced Raman scattering (SERS), extremely strong Raman scattering signals are detected, when molecules are adsorbed on noble metal nanoparticle aggregates that are illuminated at the resonance frequencies of the coupled plasmon modes of the aggregates. The SERS cross section is approximately proportional to T_2^4 if the discussion is limited within spherical particles. This indicates that we need to obtain the system yielding longest possible T_2 to maximize the local field enhancement, by adjusting the size, shape, and assembly structure of the nanoparticles [57]. In the case of our sample, the dephasing time was experimentally determined to be 8 fs. This indicates that, as far as the relation $f \propto T_2$ holds, the nanostructure studied may give higher enhancement of optical fields and SERS comparing with the spherical gold nanoparticles whose dephasing time is shorter than 5 fs, while there still remains some space to improve the enhancement, by using gold nanorods with higher aspect ratio. The ultrafast SNOM measurement method presently developed may provide valuable tool to reveal the mechanism of optical field enhancement and to design metal nanostructures possessing favorable optical characteristics.

Chapter 5

Summary and future prospects

In summary, we have developed an apparatus for ultrafast near-field microscopic measurements based on a SNOM with an apertured optical-fiber probe. To achieve very high (<20 fs) time resolution at the near-field probe tip, we tried several GVD compensator setups to compensate the dispersion arising from the fiber and compress the pulse duration. The prism pair - DFM combination setup, the grating pair - DFM combination setup, and the prism pair - grating pair - DFM combination setup were examined. We found that the former two setups could not fully remove the GVD arising from the optical elements, the optical fiber for the near-field probe in particular. This is probably because precise pre-compensation of the third-order GVD as well as the second-order one is difficult, after transmitting through 150-mm optical fiber medium, if we install only the prism pair or the grating pair.

We have found that the combination of the prism pair, the grating pair, and DFM have capability to (nearly) fully remove the GVD and almost recover the original pulse width at the probe tip. The near-field pulse duration observed was ~17 fs, which is the shortest pulse duration ever obtained in an aperture-type SNOM system.

Very recently, another group achieved generation of ~16-fs optical pulses with a sharp spatial confinement (~10 nm) by using a gold tip with a grating structure [81]. Time resolution is the same order to as that in the present study. In this method, the shortest pulse duration may be limited by the dephasing time of plasmons at the tip, since the spatial confinement is based on the plasmonic excitations. Similar result was also reported for a gold-coated glass fiber tip [82]. The present method does not have, in principle, such a limitation in the pulse width if the coating material of the probe is appropriately selected, and may have the potential to achieve near-field microscopy with an even higher time resolution (<10 fs).

We applied this high time-resolution SNOM system to observe ultrafast dephasing

of SPR in a gold nanoparticle, based on the time-correlated TPI-PL measurement. The dephasing time constant of the order of ~10 fs was obtained by the fitting procedure, which is in good agreement with the result previously reported based on the scattering spectral profile analysis. This is the fastest dynamics of a single-particle material ever observed directly in the time-domain by SNOM. Since the dephasing time of SPR is affected by the surface scattering, spatially resolved dephasing measurements for single nanostructures may yield fundamental information on the decay mechanism. As a next step, we are now conducting space-resolved plasmon dynamics measurements in individual metal nanoparticles.

A number of works have been devoted to ensemble measurements of dephasing for SPR in noble metal nanoparticles with various shapes until now. On the other hand, single-particle measurements, which are indispensable to understand dynamics of nanostructures and their shape and size dependences, are rather limited. This is probably because of difficulties in time-resolved microscopy technique. Our ultrafast SNOM technique can directly access to the dephasing of SPR in noble metal nanostructures and even have a potential to investigate the position dependence of dephasing in a single particle. Such experiment is now under way and will provide valuable information on coherence and energy dissipation of SPR in metal nanoparticles.

Most of published works on SPR have been on noble metal nanoparticles, such as gold or silver nanoparticles or composites of gold and silver, because they show prominent resonances in the visible to near-infrared region. In the future, dynamic SNOM investigation of other metallic nanostructures such as transition metal particles may also provide valuable information on electron dynamics in nanomaterials in general. In this case, further higher time resolution and/or wider tunability of the light source may be necessary.

The SNOM system of very high time resolution may also lead to the experiments of coherent control in nano-systems, including not only the metal nanoparticles but also semiconductor and other materials. Manipulation of ultrafast carrier dynamics in metallic and semiconductor nanostructures might be realized on the basis of the ultrafast SNOM systems.

References

1. S. W. Hell：Science **316** (2007) 1153.

2. T. A. Klar and S. W. Hell：Opt. Lett. **24** (1999) 954.

3. M. J. Rust, M. Bates, and X. W. Zhuang：Nat. Methods. **3** (2006) 793.

4. E. Betzig, G. H. Patterson, R. Sougrat, O. W. Lindwasser, S. Olenych, J. S. Bonifacino, M. W. Davidson, J. L. Schwartz, and H. F. Hess：Science **313** (2006) 1642.

5. S. T. Hess,T. P. K. Girirajan, and M. D. Mason：Biophys. J. **91** (2006) 4258.

6. R. E. Thompson,D. R. Larson, and W. W. Webb：Biophys. J. **82** (2002) 2775.

7. E. Abbe, Arch. Mikrosk. Anat：EntwMech **9** (1873) 413.

8. G. D. Danilatos：Adv. E. E. P. **71** (1988) 109.

9. N. Tanaka：Sci. Technol. Adv. Mater **9**, (2008) 014111.

10. K. M. Lang, D. A. Hite, R. W. Simmonds, R. McDermott, D. P. Pappas, and J. M. Martinis：Review of Scientific Instruments **75** (2004) 2726.

11. Tersoff. J and D. R. Hamann：Phys. Rev. B. **31** (1985) 805.

12. E. H. Synge：Philos. Mag. **6** (1928) 356.

13. E. A. Ash and G. Nicholls：Nature **237** (1972) 310.

14. G. Binnig and H. Rohre：IBM Journal of Research and Development **30** (1986) 355.

15. A. Lewis, M. Isaacson, A. Harootunian,and A. Muray：Ultramicroscopy **13** (1984) 227.

16. D. W. Pohl, W. Denk, and M. Lanz：Appl. Phys. Lett. **44** (1984) 651.

17. D. W. Pohl：Adv. Opt. Electron. Microsc. **12** (1991) 243.

18. A. Hagen, M. Steiner, M. B. Raschke, C. Lienau, T. Hertel, H. H. Qian, A. J. Meixner, and A. Hartschuh：Phys. Rev. Lett. **95** (2005) 197401.

19. T. W. Ebbesen, H. J. Lezec, H. F. Ghaemi, T. Thio, and P. A. Wolff：Nature **391** (1998) 667.

20. C. Ropers, D. J. Park, G. Stibenz, G. Steinmeyer, J. Kim, D. S. Kim, and C. Lienau：Phys. Rev. Lett. **94** (2005) 113901.

21. K. Imura and H. Okamoto：Opt. Lett. **31** (2006) 1474.

22. K. Imura, T. Nagahara, and H. Okamoto：Appl. Phys. Lett. **88** (2006) 023104.

23. D. W. Pohl and B. Hecht et al：Chimia **51** (1997) 760.

24. C. W. Siders, A. Cavalleri, K. Sokolowski-Tinten, C. Toth, T. Guo, M. Kammler, M. H. v. Hoegen, K. R. Wilson, D. v. Linde, and C. P. J. Barty：Science **286** (1999) 1340.

25. B. J. Siwick, J. R. Dwyer, R. E. Jordan, and R. J. D. Miller：Science **302** (2003) 1382.

26. H. Ihee, V. A. Lobastov, U. M. Gomez, B. M. Goodson, R. Srinivasan, C. Y. Ruan, and A. H. Zewail：Science **291** (2001) 458.

27. E. A. Ash and G. Nicholls：Nature **237** (1972) 510.

28. D. W. Pohl, W. Denk, and M. Lanz：Appl. Phys. Lett. **44** (1984) 651.

29. H. Okamoto and K. Imura：J. Mater. Chem. **16** (2006) 3920.

30. K. Imura and H. Okamoto：Bull. Chem. Soc. Jpn. **81** (2008) 659.

31. K. Imura and H. Okamoto：J. Am. Chem. Soc. **126** (2004) 12730.

32. K. Imura and H. Okamoto：Opt. Lett. **31** (2006) 1474.

33. K. Imura, T. Nagahara, and H. Okamoto：Appl. Phys. Lett. **88** (2006) 023104.

34. K. Imura, H. Okamoto, M. K. Hossain, and M. Kitajima：Nano Lett. **6** (2006) 2173.

35. T. Shimada, K. Imura, M. K. Hossain, H. Okamoto, and M. Kitajima：J. Phys. Chem. C. **112** (2008) 4033.

36. L. Novotny, R. X. Bian, and X. S. Xie：Phys. Rev. Lett. **79** (1997) 645.

37.   E. J. Sanchez, L. Novotny, and X. S. Xie：Phys. Rev. Lett. **82** (1999) 4014.

38.   A. Bouhelier, M. Beversluis, A. Hartschuh, and L. Novotny：Phys. Rev. Lett. **90** (2003) 013903.

39.   C. Bohren and D. Huffmann：*Absorption and Scattering of Light by Small Particles* (John Wiley, New York, 1983).

40.   U. Kreibig and M. Vollmer：*Optical Properties of Metal Clusters*, Springer Series in materials Science **125** (Springer, Berlin, 1995).

41.   H. Raether：*Surface Plasmons, Springer Tracts in Modern Physics* (Springer, Berlin, 1988).

42.   S. Kawata：*Near-field Optics and Surface Plasmon Polaritons：Topics in Applied Physics* (Springer-Verlag, Berlin, Heidelberg, 2001).

43.   S. Link and M. A.El-Sayed：Annu. Rev. Phys. Chem. **54** (2003) 331.

44.   W. S. Fann, R. Storz, H. W. Tom, and J. Bokor：Phys. Rev. B. **46** (1992) 13592.

45.   H. E. Elsayed-Ali, T. B. Norris, M. A. Pessot, and G. A. Mourou：Phys. Rev. Lett. **58** (1987) 1212.

46.   R. W. Schoenlein, W. Z. Lin, J. G. Fujimoto, and G. L. Eesley：Phys. Rev. Lett. **58** (1987) 1680.

47.   C.-K. Sun, F. Valee, L. Acioli, E. P. Ippen, and J. G. Fujimoto：Phys. Rev. B **48**, (1993) 12365.

48.   R. Rosei, F. Antongeli, and U. M. Grassano：Surf. Sci. **37** (1973) 689.

49.   A. E. Faulhaber, B. A. Smith, J. K. Andersen, and J. Z. Zhang：Cryst. Liq. Crst. **283** (1996) 25.

50.   M. Hu and G. V. Hartland：J. Phys. Chem. B **106** (2002) 7029.

51.   S. Link, M. B. Mohamed, T. Asahi, H. Masuhara, and M. A. El-Sayed：J. Phys. Chem. B **103** (1999) 3073.

52.   J. H. Hodak, I. Martini, and G. V. Hartland：J. Phys. Chem. B **108** (1998) 9210.

53. M. Scharte, R. Porath, T. Ohms, M. Aeschlimann, B. Lamprecht, H. Ditlbacher, F. R. Aussenegg：Proc. SPIE **4456** (2001) 14.

54. B. Lamprecht, A. Leitner, and F. R. Aussenegg：Appl. Phys. B **64** (1997) 269.

55. B. Lamprecht, A. Leitner, and F. R. Aussenegg：Appl. Phys. B **68** (1999) 419.

56. Y.-H. Liau, A. N. Unterreiner, Q. Chang, and N. F. Scherer：J. Phys. Chem B **105** (2001) 2135.

57. T. Klar, M. Perner, S. Grosse, G. von Plessen, W. Spirkl，and J. Feldmann：Phys. Rev. Lett. **80** (1998) 4249.

58. C. Sönnichsen, T. Franzl, T. Wilk, G. von Plessen, and J. Feldmann：Phys. Rev. Lett. **88** (2002) 077402.

59. F. Stietz, J. Bosbach, T. Wenzel, T. Vartanyan, A. Goldmann, and F. Trager：Phys. Rev. Lett. **84** (2000) 5644.

60. C. Rulliere：*Femtosecond Laser Pulses*：*Principles and Experiments* (Springer, Berlin, 2005) 2nd ed.

61. C. A. Schmuttenmaer, M. Aeschlimann, H. E. Elsayed-Ali, R. J. D. Miller, D. Mantell, J. Cao, and Y. Gao：Phys. Rev. B **50** (1994) 8957.

62. M. Aeschlimann, M. Baure, and S. Pawlik：Chem. Phys. **205** (1996) 127.

63. M. Wolf：Surf. Sci. **343** (1997) 377.

64. B. Lamprecht, J. R. Krenn, A. Leitner, and F. R. Aussenegg：Appl. Phys. B **69** (1999) 223.

65. L. B. A.Leitner and F. R. Aussenegg：Appl. Phys. B **68** (1999) 419.

66. R. L. Fork, O. E. Martinez, and J. P. Gordon：Opt. Lett. **9** (1984) 150.

67. E. B. Treacy：IEEE J. Quantum. Elect. **QE-5** (1969) 454.

68. A. M. Weiner, D. E. Leaird, J. S. Patel, and J. R. Wullert：IEEE J. Quantum. Elect. **28** (1992) 908.

69. M. A. Dugan, J. X. Tull, and W. W. Warren：J. Opt. Soc. Am. B **14** (1997) 2348.

70. E. Zeek, K. Maginnis, S. Backus, U. Russek, M. Murnane, G. Mourou, H. Kapteyn, and G. Vdovin：Opt. Lett. **24** (1999) 493.

71. R. H. Stolen and Lin. Q：Phys. Rev. A **17** (1978) 1448.

72. Anderson. D, M. Desaix, M. Lisak, and M. L. Quiro-Teixeriro：J. Opt. Soc. Am. B **9** (1992) 1358.

73. W. Sellmeier：Annalen der Physik and Chemie **219** (1871) 272.

74. J. W. Fleming：Appl. Opt. **23** (1984) 4486.

75. G. P. Agrawal：*Applications of Nonlinear Fiber Optics,* (Academic Press, Burlington, 2001) 2nd ed.

76. M. S. Kovacevic and A. Djordjevich：J. Opt. Adv. Mat. **14** (2012) 198

77. J.-C. Diels and W. Rudolph：*Ultrafast Laser Pulse Phenomena,*. (Academic Press - Elsevier, New York, 2006) 2nd ed.

78. J. H. Holland：*Adaptation in Natural and Artificical system*, (U. of Michigan Press, Ann Arbor,1975).

79. M. Gen and R. Cheng：*Genetic Algorithms and Engineering Design* (Wiley, New York, 1997).

80. C. Sönnichsen, S. Geier, N. E. Hecker, G. vonPlessen, J. Feldmann, H. Ditlbacher, B. Lamprecht：Appl. Phys. Lett. **77** (2000) 2949.

81. S. Berweger, J. M. Atkin, X. G. Xu, R. L. Olmon, and M. B. Raschke：Nano Lett. **11** (2011) 4309.

82. K. Furusawa, N. Hayazawa, T. Okamoto, T. Tanaka, and S. Kawata：Opt. Express. **19** (2011) 25328.

Acknowledgement

74

A lot of appreciations also go to the secretary Ms. Emiko Nomura. She helped me solve a lot of daily life problems when I lived in Japan. Without her help, my stay in Japan will become very difficult.

Finally, I would like to thank my parents and sister. It is just their love and encouragement that I could finish this study.